Sagol School of Neuroscience

Department of Biomedical Engineering

The Iby and Aladar Fleischman Faculty of Engineering

Ultrasound-mediated Blood-brain-barrier Opening for the Delivery of mRNA-Lipid Nanoparticles in a Glioblastoma Mouse Model

By

Maya Elbaz

The thesis was carried out under the supervision of

Dr. Tali Ilovitsh

October 2024

בית הספר סגול למדעי המוח

הפקולטה להנדסה ביו-רפואית ע"ש איבי ואלדר פליישמן

פתיחת מחסום-דם-מוח ע"י אולטרסאונד להעברה של ננו-חלקיקים ליפידיים עם מטען רנ"א במודל עכברי של גליובלסטומה

מאת

מאיה אלבז

החיבור בוצע בהנחייתה של

ד"ר טלי אילוביץ

אוקטובר 2024

Acknowledgments

I would like to thank the following people:

Dr. Tali Ilovitsh, my supervisor, for her unwavering support and professional guidance throughout my research journey, both intellectually and personally.

Special thanks to Dr. Mike Bismuth for his invaluable assistance as our lab manager, and to all the members of the Ilovitsh lab for insightful discussions and collaborations.

Most of all, I would like to dedicate this thesis to my beloved family and my husband, Ravid Shumer, for continually believing in me, supporting me and motivating me to persevere. Their endless encouragement allowed the completion of this work.

Abstract

Lipid-nanoparticles (LNPs) are FDA-approved non-viral RNA delivery systems for gene therapy and immunotherapy. However, their application for brain therapy is hindered by the restrictive blood-brain-barrier (BBB). Focused ultrasound (FUS) combined with microbubbles (MBs) is a leading approach to disrupt the BBB in a local, safe, and transient manner, also known as 'BBB opening' (BBBO). Yet, delivering large particles remains a challenge, as it requires striking a fine balance between increasing peak negative pressures (PNPs) and maintaining microvasculature integrity. Here, we challenged their size-dependent delivery paradigm. We carefully optimized low-frequency ultrasound parameters to induce sufficiently high amplitude MBs oscillations, facilitating the systemic delivery of a range of large molecules, including lipid nanoparticles, across the BBB without causing tissue damage. Initially, BBBO was evaluated across various center frequencies (850, 250, 80 kHz) and PNPs by monitoring the extravasation of the BBB integrity marker Evans blue (EB) (~1 kDa). Then, delivery of various-sized particles, including: 4, 70 and 150 kDa Dextrans, siRNA-Cy5-LNP (~70 nm) and mRNA-luc-LNP (~100 nm) was assessed using fluorescent microscopy and bioluminescence. Lastly, we demonstrated the successful delivery of siRNA-Cy5-LNP in an aggressive glioblastoma 005 mouse model. Our results revealed that in a mouse model, the optimized parameters of a center frequency of 850 kHz and a PNP of 125 kPa induced safe BBBO, enabling the delivery of both small molecules and large LNPs. In healthy brains, ultrasound-mediated BBBO for siRNA-Cy5-LNP delivery resulted in a 10-fold signal increase compared to control brains. Similarly, mRNA-luc-LNP delivery following BBBO demonstrated a 12-fold increase in luciferase enzyme expression 24 hours post-treatment, compared to controls. Finally, applying the optimized parameters to deliver siRNA-Cy5-LNP in a glioblastoma mouse model yielded a 6.7-fold increase compared to the sham group. This study paves the way for non-invasive LNPs delivery to the brain, offering a versatile platform for the treatment of brain malignancies, as well as neurodegenerative diseases.

List of Publications:

- **M. Elbaz**, N. Ad-El, Y. Chulanova, D. Brier, M. Goldsmith, M. Bismuth, A. Brosque, D. Sher, A. Gutkin, D. Bar-On, D. Friedman-Morvinski, D. Peer, T. Ilovitsh. "Low-frequency ultrasound-mediated blood-brain barrier opening enables non-invasive lipid nanoparticle delivery to glioblastoma" (2024, Under Review). First author contribution: Wrote the original draft, created the visualizations and contributed to editing and reviewing of the manuscript; Conducted all the BBBO experiments in this study, including optimizations of the therapeutic setup, microscopy, and staining techniques; Conducted the in-vitro and in-vivo experiments and prepared microbubbles; Performed the data acquisition, analysis and validation.

Conference Presentations:

- **M. Elbaz**, N. Ad-El, Y. Chulanova, D. Brier, M. Goldsmith, M. Bismuth, A. Brosque, D. Sher, A. Gutkin, D. Bar-On, D. Friedman-Morvinski, D. Peer, T. Ilovitsh. "Ultrasound-Mediated Blood Brain Barrier Opening for the Delivery of mRNA Lipid Nanoparticles in a Glioblastoma Mouse Model", IEEE IUS, Taiwan, September 2024. (Oral presentation)

- **M. Elbaz**, N. Ad-El, Y. Chulanova, D. Brier, M. Goldsmith, M. Bismuth, A. Brosque, D. Sher, A. Gutkin, D. Bar-On, D. Friedman-Morvinski, D. Peer, T. Ilovitsh. “Ultrasound-mediated blood brain barrier opening for the delivery of mRNA lipid nanoparticles in a glioblastoma mouse model”, ISTU, Taiwan, September 2024. (Student Award Poster presentation)

Patent:

- **M. Elbaz**, M. Goldsmith, D. Peer and T. Ilovitsh. "Method To Noninvasively Deliver Lipid Nanoparticles To The Brain Using Ultrasound-Mediated Blood Brain Barrier Opening", US Provisional Patent Application No. 63/691,874**.**

Contents

Acknowledgments....3
Abstract ……..……..4
List of Publications: 5
Abbreviations and symbols....8
List of figures....9
1. Introduction....10
2. Research hypothesis and objectives....13
3. Scientific background 15
3.1. The blood-brain barrier 15
.3.2 BBBO visualization and quantification 17
3.3. Ultrasound principles....18
3.4. Low frequency ultrasound 20
3.5. Clinical ultrasound brain therapy....20
3.6. Microbubbles 22
3.7. FUS-mediated BBBO 23
3.8. LNPs-based therapy....25
3.9. Glioblastoma: disease and therapy....27
4. Methods and materials 30
4.1. Microbubble preparation....30
4.2. RNA-LNP preparation & characterization 31
4.3. In vitro RNA-LNPs transfection assay 31
4.4. In-Vivo BBBO Experiments....32
4.5. Glioblastoma 005 orthotopic model....35
.4.6 Microscopy imaging and Quantitative analysis....36
5. Results....38
5.1. LNP characterization and in-vitro transfection....38
5.2. Low-Frequency mediated BBBO in healthy mice....40
5.2.1. FUS center-frequency optimization and selection....40
5.2.2. FUS-mediated BBBO in 850 kHz....42
5.2.3. 250 vs. 850 kHz center-frequency 48
5.3. Glioblastoma mouse model....49
5.3.1. siRNA-Cy5-LNPs delivery....49
6. Discussion....51
7. Final conclusions and future work....56

8. References......57
.9 תקציר......65

Abbreviations and symbols

BBB ……...…… Blood-brain-barrier	**kPa**……..... kilopascal
BBBO ...……..... Blood-brain-barrier opening	**LNP…...**…...…….....…Lipid nanoparticles
EB ……...…..... Evans Blue	**LUC** ……. Luciferase (enzyme)
FDA……..... Food and drug administration	**MB**……..…….……... Microbubble
FITC ….……..... Fluorescein isothiocyanate	**MRI** ….....…Magnetic resonance imaging
FUS.….……...…… Focused ultrasound	**mRNA**…..……...……...messenger RNA
GBM ….……..……. Glioblastoma	**Mw** ……...……..... Molecular weight
GFP…… Green fluorescent protein	**NTC**……. No treatment control
H&E……..…... Hematoxylin and eosin	**PBS** …….……. Phosphate buffered saline
IACUC ..... Institutional Animal Care and Use Committee	**PBS (+/+)**…….…... Phosphate buffered saline containing calcium and magnesium
IHC……....…….. Immunohistochemistry	**PNP** …….…..... Peak negative pressure
IV ……...…....…….…….. Intra-venous	**PRF** ……..... Pulse repetition frequency
IVIS……...…….**.....** In-vivo imaging system	**RH**…….……..... Right hemisphere
kDa ……..…….…. kilodalton	**siRNA**……..……small interference RNA

List of figures

Figure 1: Overview of the non-invasive brain delivery and quantification platform..14

Figure 2: The neurovascular unit 16

Figure 3: BBBO visualization and quantification 17

Figure 4: Biological effects of FUS and intracranial applications in humans …….. 21

Figure 5: Microbubbles ultrasound contract agents 23

Figure 6: FUS mediated BBBO combined with microbubbles 24

Figure 7: Structure of cationic liposomes versus Lipid Nanoparticles (LNPs) …..... 25

Figure 8: Mechanism of mRNA-LNPs intracellular uptake 26

Figure 9: Varying levels of BBB integrity inside glioblastoma tumor 28

Figure 10: Microbubbles size distribution and concentration..... 30

Figure 11: Experimental ultrasound setup..... 33

Figure 12: Illustration of ionizable LNPs: structure and cargo..... 38

Figure 13: LNPs: size distribution, concentration and zeta potential measurement... 39

Figure 14: LNPs evaluation of in-vitro transfection.....40

Figure 15: EB extravasation post FUS-BBBO as a function of center-frequency…. 41

Figure 16: EB extravasation as a function of PNP at 850 kHz ……..... 42

Figure 17: Delivery of EB and 4-150 kDa fluorescent dextran (850 kHz) 44

Figure 18: Safety evaluation of siRNA-Cy5-LNPs delivery (850 kHz) 45

Figure 19: siRNA-Cy5-LNPs brain delivery in healthy mice (850 kHz) ……...,.... 46

Figure 20: mRNA-luc-LNPs brain delivery in healthy mice (850 kHz) .....,..... 47

Figure 21: Luciferase protein expression post 24 hours (250 vs. 850 kHz)…...…..... 49

Figure 22: Delivery of siRNA-Cy5-LNP into glioblastoma tumors (850 kHz)..... 50

1. Introduction

The BBB is a crucial defense mechanism protecting the brain from pathogens and toxins, yet at the same time poses a significant challenge to the delivery of therapeutics into the brain for the treatment of neurological conditions[1–4]. Glioblastoma (GBM) is the most common and aggressive primary brain malignancy, with a median survival of approximately 15 months following treatments[5]. According to the national brain tumor society, GBM has an incidence rate of two to three per 100,000 adults per year worldwide, and it accounts for 12-15% of all intracranial tumors and 50-60% of astrocytic tumors. Although the BBB may be compromised in regions affected by the tumor, this disruption is often irregular and not uniformly distributed across the entire tumor mass[5,6]. Additionally, the extent of BBB compromise is stage-dependent; in the early stages of GBM, the BBB remains relatively intact, preventing the effective passage of large therapeutic agents, including chemotherapies and antibodies[4,7]. Currently, the widely accepted protocol to treat GBM is a combination of the chemotherapy temozolomide, radiation therapy, and invasive surgical resection of the tumor, and it has remained largely unchanged for several years[5]. The high recurrence rates (>90%) and dismal five-year survival rates (6.8%) highlight the need for advanced delivery systems capable of effectively transporting therapies across the BBB and into the tumor[8]. The goal in this research is to develop a non-invasive method for delivering LNPs across the blood-brain barrier, offering a novel therapeutic platform for GBM treatment.

LNPs represent an advanced and FDA-approved form of non-viral RNA delivery system for gene therapy and immunotherapy[9]. In particular, the latest generation of LNPs incorporating ionizable lipid helpers exhibit improved encapsulation and transfection efficiency of both short siRNA and long mRNA nucleic acids sequences[10]. Among their advantages are enhanced target specificity, good biodegradability, heightened protein expression, increased therapeutic efficacy and manageable immunogenicity. Consequently, LNPs represent a promising avenue for treating various pathologies through genetic manipulation. Lately, they had been FDA-approved for the indications of Hereditary transthyretin amyloidosis (hATTR) Onpattro® and the mRNA-based COVID-19 vaccines by Moderna and Pfizer-BioNTech[10,11].

In cancer therapy, LNPs offer a promising strategy for gene manipulation,

specifically, by delivering modified messenger RNA. The suppressed immune system in cancer patients is characterized by lower T cell counts, less effector immune cells infiltration, higher levels of exhausted effector cells and higher levels of immunosuppressive cytokines, such as TGF-β[13]. Pro-inflammatory cytokines have been shown to promote anti-tumor immune responses, by promoting peripheral T cell expansion and counteracting the immunosuppressive network, inducing potent tumor regression and increase overall survival in various tumor models[12]. However, a significant limitation of this strategy lacks effective and specific delivery methods, which can lead to severe systemic adverse reactions. LNP-mediated delivery of pro-inflammatory cytokines directly to the tumor site has the potential to reduce systemic adverse reactions and improve therapeutic outcomes. Therefore, certain pro-inflammatory cytokines hold significant therapeutic potential, making the development of such delivery systems crucial.

While LNPs emerge as promising carriers for gene therapy, their applications in advanced brain therapies are impeded by limited permeability across the BBB, and previous studies utilizing LNPs to treat brain diseases often resort to direct administration into the brain tumor via stereotaxic injection[13]. Here, we aim to establish the use of low-frequency FUS combined with MBs for the non-invasive delivery of LNPs across the BBB and into the tumor. The method relies on MBs as biocompatible ultrasound contrast agents which are FDA approved for use in humans[14]. The most common MBs are composed of lipid-shell and a gas core with an average radius of 0.75 μm[15]. Upon excitation with FUS, the MBs cavitate, expanding their radius and exerting temporary mechanical forces on adjacent cell membranes. When this process occurs within blood vessels in the brain, the BBB endothelium can open safely and transiently, facilitating the local delivery of particles into the brain parenchyma, that would otherwise be excluded[16,17].

BBBO has been extensively validated through the administration of a diverse array of small molecules for both imaging and therapeutic applications in the brains of rodents and non-primates[18–21]. These studies have consistently demonstrated safe and efficient delivery with minimal off-target effects. Moreover, in recent years, clinical trials are ongoing across spectrum of neurological conditions, including Alzheimer's disease, Parkinson's disease, psychiatric disorders, and chemotherapy/antibody-based treatments in GBM[22–26].

Despite the significant progress that has been achieved in therapeutic FUS-mediated BBBO, effective delivery of large nanocarriers for advanced brain therapies, remains a persistent challenge. Previous efforts to transport genetic payloads using FUS-mediated BBBO, have explored various nanoscale methods, including viral vectors[27,28], liposomes[29,30], colloidally stable pDNA-NP[31], and even stem-cells[32]. A primary challenge associated with delivering nanoscale particles through the BBB lies in balancing the required PNPs to effectively open the barrier while maintaining microvasculature integrity. Higher PNPs are often necessary for delivering large particles, which can lead to undesired microhemorrhages[33]. This is because higher PNPs induce greater MB oscillations, which can create larger gaps in the BBB, facilitating the delivery of larger molecules[34]. Nonetheless, increasing PNP raises the risk of MBs transitioning from stable cavitation, where they oscillate without collapsing, to inertial cavitation, where the bubbles collapse violently, generating microjets that can cause microhemorrhages and brain tissue damage[34,35]. Notably, previous delivery of stem cells (~6 μm) has been reported to induce such transient microhemorrhage[32].

In this research, we aim to optimize low-frequency ultrasound parameters to induce high-amplitude MBs oscillations, enabling the systemic delivery of large molecules across the BBB without causing tissue damage. Our focus is on delivering LNPs with the potential to encapsulate cytokine modifying mRNA to manipulate gene expression in GBM. More broadly, this approach offers a promising, non-invasive platform for delivering LNPs to the brain, with versatility stemming from the ability to alter the therapeutic RNA cargo, enabling their investigation across a wide range of brain therapies.

2. Research hypothesis and objectives

Our hypothesis is that low-frequency ultrasound mediated BBB combined with MBs can be used for the non-invasive delivery of LNPs (~100nm) encapsulating modified messenger RNAs in GBM mouse model.

The specific aims are as follows:

- Aim 1: Optimize low-frequency FUS-mediated BBBO with MBs for enhanced brain delivery of various-sized large particles (fluorescent dextrans).
- Aim 2: Establish safe delivery of two types of LNPs (siRNA-Cy5 and mRNA-luc) across the BBB in healthy mice.
- Aim 3: Analyze LNPs accumulation into the tumor region in GBM mouse model using our method.

Driven from the aims, the work was structured as follows; We first validated the safe operation region for BBBO in normal mice with an intact BBB across various center frequencies (850, 250, 80 kHz) and PNPs (500 - 125 kPa) by monitoring the extravasation of EB (~1 kDa). The safety of treatments was assessed via pathology and five veterinary health measures. Then, the optimized FUS parameters were used for the delivery of different-sized fluorescent dextrans (4 - 150 kDa) and Cy5 labeled siRNA-LNP, evaluating their brain distribution via fluorescent microscopy. Luciferase mRNA encapsulating LNPs were used to assess distribution in whole brains through evaluation of luminescence signal in whole animal using in-vivo imaging system (IVIS).

Moving on to the GBM mouse model, mice were inoculated with 005 GBM cells and monitored for tumor growth using IVIS. After ~21 days, mice were systemically injected with siRNA-Cy5-LNPs following treatment with FUS-mediated BBBO. Tumor accumulation of the fluorescently labeled LNPs was confirmed in brain histology and marker's intensity was quantified (Fig. 1).

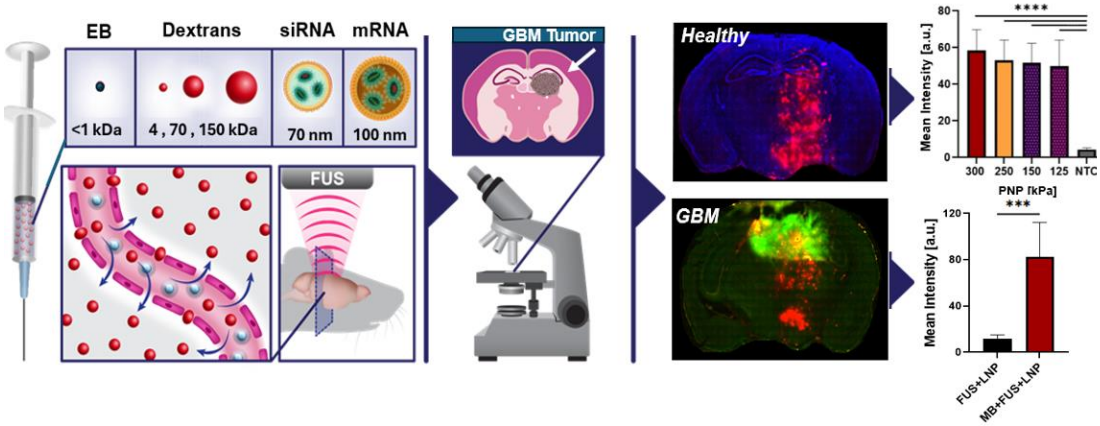

Figure 1. Overview of the non-invasive brain delivery and quantification platform. BBBO was induced using MBs and low-intensity FUS targeted to the right hemisphere. Each time, the mice were systemically injected with one of six particles with progressively increasing size (1, 4, 70, and 150 kDa or 70 and 100 nm) and particles extravasation was quantified using fluorescent microscopy, in healthy brains and in GBM tumors.

3. Scientific background

This thesis investigates using low-frequency FUS combined with MBs to non-invasively deliver RNA-based LNPs across the BBB. The research focuses on GBM, an aggressive brain cancer with limited treatment options. By leveraging low FUS-mediated BBBO, the study aims to enhance the delivery of RNA-based LNPs, which can modify gene expression and stimulate the immune system to target tumors. This method has potential applications beyond GBM, offering a versatile approach for RNA-based therapies in various neurological disorders.

In this section, we will delve into the key components of this therapeutic approach. First, we will introduce the BBB architecture, highlighting the challenges it poses for the delivery of large particles to the brain. Next, we will discuss the principles underlying the FUS-mediated BBBO procedure, explaining the motivation behind this platform and its potential to promote brain treatments. We will explore the physical concepts that underpin this ultrasound method, including the basics of ultrasound as a tool for both imaging and therapy, and the role of MBs as enhanced contrast agents. Following this, we will examine the properties of LNPs, emphasizing their potential for gene manipulation therapies, and review their current status in pre-clinical and clinical development. Finally, we will provide an overview of GBM brain tumors, setting the stage for understanding the disease and its challenges.

By the end of this section, the reader should have a clear understanding of the mechanisms behind FUS-mediated BBBO for large particles delivery, the therapeutic potential of LNPs, and the complexities of GBM. This foundation will prepare the reader for a deeper exploration of the research questions addressed in this work.

3.1. The blood-brain barrier

The brain is one of the most vital organs in the human body, consuming a significant portion of our metabolic resources[1]. To meet its high demand for nutrients, the brain relies on an extensive network of blood vessels, primarily composed of capillaries, which are the main sites for substance exchange between the blood and brain tissue. The functionality of the BBB relies on a precise and strict architecture to maintain the delicate chemical balance required for proper brain function and to protect against pathogens and toxins. This barrier is formed by non-fenestrated brain endothelial cells

lining the walls of CNS blood vessels, along with pericytes, neurons, and glial cells, collectively known as the "neurovascular unit" (NVU), which provides integrity to the BBB (Fig.2).

Studies have shown that the tight junctions in the endothelial cells of brain capillaries are more restrictive than those in other parts of the body[35]. Specifically, the CNS endothelial cells are held by abundance of tight junction proteins (e.g.: claudins and occludins) and adhesion complexes (e.g.: ZO-1 and ZO-2), which create a high-resistance paracellular barrier. Additionally, the wide expression of efflux transporters, such as Mdr1, BCRP, and MRPs, further reinforces the BBB by actively transporting small lipophilic molecules out of the endothelial cells, preventing their passive diffusion through their membranes. Thus, both paracellular and transcellular barriers can be strictly controlled[2].

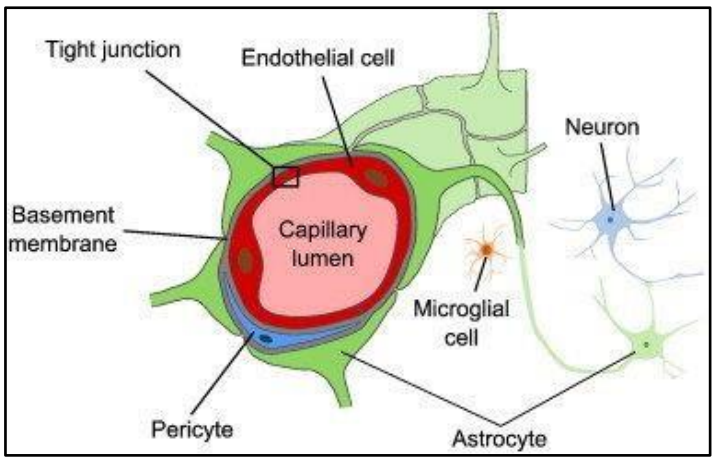

Figure 2. The neurovascular unit; consists of various cells encircling the brain capillary, which, along with restrictive tight junctions, form the BBB. *Illustration adopted from Heye et al.* (2014)[36].

While incredibly important for proper physiological brain activity, the BBB poses a major challenge for delivering therapeutics needed to treat neurological conditions[4]. Over time, various strategies have been proposed and tested to overcome the BBB and facilitate non-invasive drug delivery to the brain. Many of these approaches involve pharmacological methods that exploit the body's natural mechanisms for crossing the BBB to deliver specific molecules. While some of these methods are effective, they often lack spatial and temporal precision, which can result in the unintended exposure of the entire brain to therapeutic agents, increasing the risk of off-target effects and potential damage.

3.2. BBBO visualization and quantification

To assess the effectiveness of any method for BBBO to enhance uptake into the brain, it is essential to establish a reliable measure of BBB integrity (Fig.3). Historically, simple dyes, such as EB, were among the first markers used for this purpose. These dyes are introduced into the bloodstream of model animals by intravenous administration and circulate to the brain's vascular system. Due to their molecular size and formulation, they cannot penetrate an intact BBB but will pass through if the barrier is compromised. Thus, the presence of the dye in the brain parenchyma serves as an indicator of BBBO[37].

The extravasation of these markers is typically measured ex-vivo. EB is particularly convenient because its extravasation occurs rapidly, requiring only a short circulation time, and the dye's presence in the brain parenchyma can be easily visualized with the naked eye, therefore is still commonly used nowadays. For other dyes, quantification may be conducted through brain tissue sectioning and subsequent fluorescent microscopy, or by chemical extraction of the dye from the collected brain tissue and volumetric analysis[38].

Acquisition of temporal data of the BBBO process is of high importance. In recent years, magnetic resonance imaging (MRI) contrast agents - such as Gadolinium, have gained popularity for visualizing and quantifying BBBO. The reason is that these agents, which permeate the brain parenchyma following BBBO, allow for in vivo visualization without the need for animal scarification, enabling the study of BBBO in real-time and following consecutive treatment cycles[39,40].

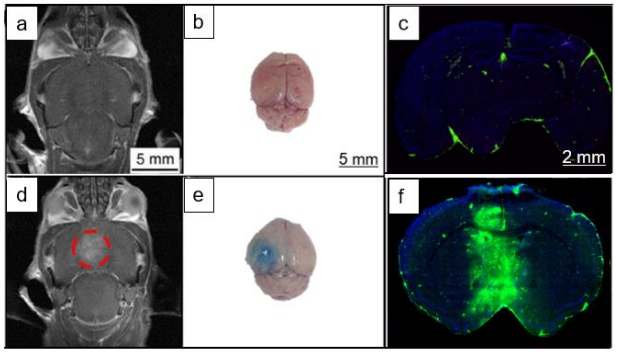

Figure 3. BBBO visualization and quantification: From the left (a,d): Real-time in-vivo visualization of BBBO using Gadolinium-enhanced MRI; *Illustration adapted from Ilovitsh et al.*, (2018)[41]. Middel to right: Ex-vivo visualization of BBB opening using: EB dye (b,e) and FITC-dextran (c,f) (*Elbaz et al.* (2024), under review). Controls are shown in (a,b,c), whereas (d,e,f) indicate BBBO.

3.3. Ultrasound principles

Ultrasound is a general term referring to sound waves with frequencies exceeding 20 kHz, above the range of human hearing. Like ordinary sound, ultrasound travels as pressure waves, causing fluctuations as it moves through a medium. An important advantage of ultrasound radiation is its non-ionizing nature, ensuring the exposure to ultrasound is safe. Ultrasound also provides relatively good depth penetration within soft tissues. Compared to other imaging modalities, such as magnetic resonance imaging (MRI) and computed tomography (CT), ultrasound devices are portable and cost-effective to manufacture. These properties make ultrasound a popular choice for both imaging and various therapeutic applications in clinic[42].

Ultrasound waves can be generated using a system comprising of two main components: an ultrasound transducer and a function generator. The transducer contains one or more piezoelectric elements that convert alternating electrical signals into pressure waves, and vice versa. The function generator produces an electrical signal with a specific frequency and amplitude, which the transducer then converts into ultrasound waves. As these waves propagate within a body, they encounter varying tissue environments, which influence their behavior. The ultrasound signal in different tissues can be absorbed, reflected, or scattered. When the ultrasound wave encounters a complex structure, an echo is produced and travels back to the transducer. This echo is then converted into an electrical signal, and the time it takes to return helps determine the location of the structure, allowing for image reconstruction[43].

The resulting image provides a cross-sectional view of anatomical structures in real-time. This imaging modality is widely used for 2D visualization of organs, aiding in the diagnosis of heart valve issues, gallbladder or kidney stones, ocular pathologies, and the detection of abnormal tissues such as tumors or cysts. Ultrasound is particularly important in pregnancy monitoring, where it enables detailed anatomical evaluation of fetal development from the early weeks of gestation. Conventional diagnostic ultrasound scanners operate at frequencies ranging from 2 to 10 MHz[43].

On another case, if the ultrasound wave is absorbed rather than reflected, it causes vibration of particles within the tissue, leading to a rise in temperature. This thermal effect of ultrasound has been recognized since the 1940s, and is commonly used in physiotherapy to warm tissues, especially joints, promoting healing and tissue modulation[44]. Additionally, when the temperature rapidly rises above 56°C, tissue

necrosis occurs, a principle that is utilized in the thermoablation of pathological tissues. High-Intensity Focused Ultrasound (HIFU) is the utilization of concentrated high energy towards a specific area, leading to thermalablation of tissue, especially tumors[45]. Commercial HIFU devices are available and used to treat conditions like breast, uterine, and prostate tumors. Beyond thermal effects, HIFU can induce non-thermal mechanical effects[43]. In this context, another routine clinical application of HIFU is the operation of short pulses of focused ultrasound for: lithotripsy, where these pulses disintegrate kidney stones, facilitating their natural clearance from the urinary tract, or for thrombolysis where it is used to break down blood clots[46,47]. The dominance of each effect is modulated by ultrasound parameters (e.g., intensity and frequency) and the type and properties of the tissue[43].

Besides these effects that rely solely on ultrasound energy, other techniques combine contrast agents, such as biocompatible gas bubbles, that are systemically injected and circulate in the blood vessels. Then, upon exposure to external ultrasound focused at a certain body area, the bubbles are activated only at that area, responding to the changing pressures by compressing and expanding their radius, without the bubbles collapsing. This physical condition is referred to as "stable cavitation". The oscillations generate temporal mechanical forces on cell membranes, compromising cell permeability and tissue integrity, in a temporal manner and increasing uptake of drug therapies. Alternatively, when ultrasound parameters lead to the expansion and subsequent collapse of bubbles, this phenomenon, known as 'inertial cavitation,' generates microjets that cause tissue damage and can be employed for mechanical ablation using bubbles[48,49].

All the above-mentioned effects rely on a good penetration of the ultrasound signal to the desired tissue and a good overlap with the desired region. Attenuation is a term referring to the reduction in amplitude of ultrasound signal. While soft tissues have minimal attenuation, hard tissues such as the bones or the teeth pose a technical challenge for ultrasound applications due to attenuation of acoustic waves. Specifically, the human skull, which can be up to 8.5 mm thick in adults, poses a considerable barrier to ultrasound in brain applications[50].

3.4. Low frequency ultrasound

In recent years, the development of low-frequency ultrasound has become particularly crucial to the advancement of ultrasound-based brain therapies. Low-frequency ultrasound usually refers to frequencies below 1MHz. These frequencies are not suitable for imaging purposes; however, they play a key particularly in brain therapeutic applications. Lower frequencies facilitate precise focusing through the human skull to a specific area, with minimal attenuation and distortion compared to higher frequencies[51].

In general, skull attenuation is directly correlated with ultrasound frequency: Higher frequencies result in greater attenuation, while low frequencies reduce this attenuation. Thus, low frequencies significantly improve the penetration of ultrasound energy through the skull. For example, while ultrasound penetration through the skull at frequencies used for imaging (2-10 MHz) is negligible, reducing the frequency to 250 kHz allows higher yield of the ultrasound energy to pass through an intact skull[41]. When used in combination with contrast agents, this significantly contributes to amplifying the therapeutic effects of both nano and micro-sized bubbles by promoting high-amplitude oscillations at relatively lower pressures than conventional MHz-range ultrasound. In addition, this frequency range also enables a broader focal area, allowing treatment of more extensive tissue volumes. Moreover, low-frequency ultrasound minimizes trans-skull distortions, making it especially valuable for brain therapies where deeper skull penetration and reduced tissue attenuation are essential[52].

3.5. Clinical ultrasound brain therapy

When the ultrasound wave passes through the skull and is focused on a specific area, bioeffects can be achieved that lead to brain treatment. These effects are varied and include: Thermoablation, transient BBBO and neuromodulation[22] (Fig. 4).

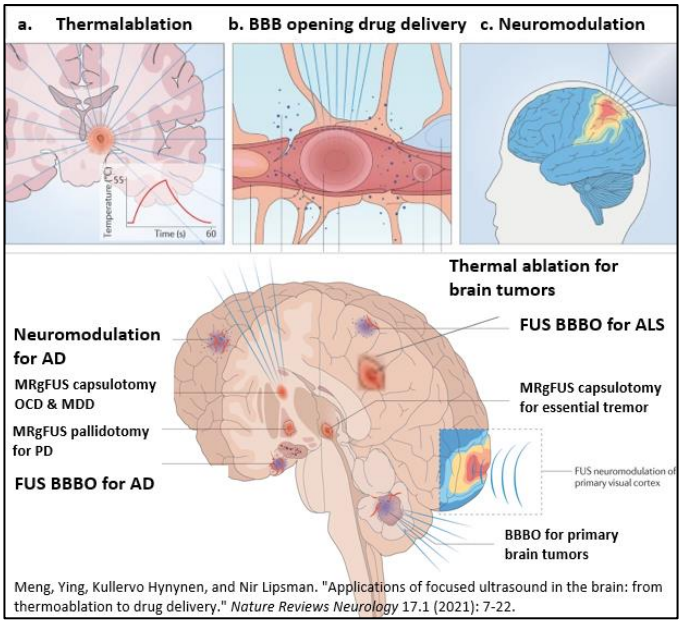

Figure 4. Biological effects of FUS (a-c) and intracranial applications in humans. *Illustration adapted from Meng et al.* (2021)[22].

In brain therapies, HIFU is employed to create precise, coagulative necrotic lesions through the intact skull, for 'incisionless neurosurgery'. This method is FDA-approved for treating essential tremor (ET) and tremor-dominant Parkinson's disease (TDPD) and is increasingly recognized as a standard of care. It is also investigated in humans in ablative procedures to disrupt pathological brain circuits in conditions such as obsessive-compulsive disorder (OCD), major depressive disorder (MDD), chronic neuropathic pain and epilepsy, offering a less invasive alternative to traditional surgical methods with promising pilot study results. Compared with existing methods like transcranial magnetic stimulation (TMS) and deep brain stimulation (DBS), this noninvasive method minimizes surgical risks while providing superior spatial and temporal resolution into deep brain regions with millimetric accuracy[22].

A different technique is FUS-mediated BBBO which relies on lower intensities that do not cause temperature rise or tissue damage; temperatures reported are at least three magnitude order below those necessary for thermoablation[21]. Under certain parameters, FUS can induce stable cavitation of exogenously injected MBs within the blood vessels which temporarily increases the permeability of the BBB. This enhanced permeability allows for targeted drug delivery directly to the brain. Furthermore, FUS-mediated BBBO has the potential to disrupt the immune-privileged status of the CNS, which can promote the initiation of an antitumor immune response and could also aid

in the detection of tumor circulating cells or their excreted antigens in the blood stream, aiding in development of non-invasive brain "sonobiopsy" tools[53].

3.6. Microbubbles

MBs are gas-filled particles with micrometer-sized diameters, initially created for ultrasound imaging because of their high echogenicity[37]. The most common MBs consist of a lipid shell with a fluorinated gas core, with an average radius of 0.75 μm[15] (Fig. 5A,B). MBs are biocompatible; they have a diameter smaller than a red blood cell and high elasticity, allowing them to freely circulate in the blood vessels through small capillaries and reach different target organs, while the gas is cleared by the lungs[38]. Over the years, MB formulations have been optimized to produce uniformly sized bubbles that can be safely administered into a patient's bloodstream, with commercial formulations now regularly employed in clinical settings[14].

MBs have a unique property that when excited by ultrasound, they can repeatedly expand and contract, in a process known as 'cavitation', being exploited for therapeutic applications via variety of mechanisms (Fig. 5C,D); At relatively low pressures, cavitation occurs stably, allowing the continuous mechanical forces exerted by the MBs on neighboring physiological barriers and cell membranes to be utilized as a therapeutic tool for targeted drug delivery and to penetrate these barriers (e.g.: BBB). On another phase, known as 'inertial cavitation,' which occurs at higher pressures, the MBs collapse, generating microjets that can disrupt tissue, making this process useful for microsurgery of cancerous tissues[54,55].

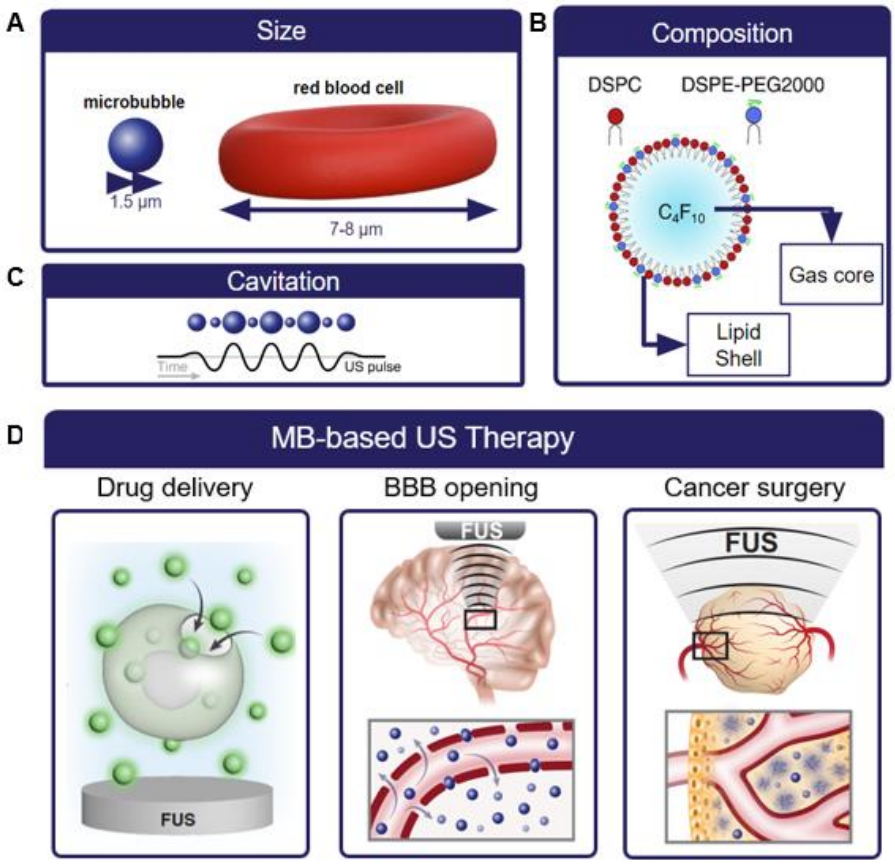

Figure 5. Microbubbles ultrasound contrast agents; Illustration of: (A, B) MBs size and composition. (C) MB Cavitation in exposure to ultrasound. (D) MB-based US therapies: Drug delivery and BBBO (by mechanism of 'stable cavitation' where bubbles oscillate and enhance penetration) and Cancer surgery (by mechanism of 'Inertial cavitation' where bubbles collapse).

3.7. FUS-mediated BBBO

As the interest in using FUS for therapeutic applications grew, researchers began to uncover its physiological effects on the brain. Among the more intriguing discoveries was the ability of FUS, when combined with MBs and specific ultrasound parameters, to induce localized, non-lethal disruptions of the BBB in targeted regions of the brain. This phenomenon, now understood to be driven by acoustic cavitation, took nearly three decades to be fully appreciated.

In FUS-mediated BBBO, intravenously injected MBs circulate freely in the bloodstream, including within the brain's vasculature. By exposing a specific brain region to transcranial ultrasound, the MBs within this area undergo cavitation, expanding and exerting temporary mechanical forces on adjacent cell membranes. This mechanical effect disrupts the tight junctions of the BBB, enhancing the penetration of

particles into the brain parenchyma that would otherwise be excluded[16,17]. Numerous studies have consistently demonstrated that this method enables safe and efficient delivery of therapeutic agents to the brain, with minimal off-target effects in both and non-primates' models [18–21]. In recent years, clinical trials have expanded to explore FUS-mediated BBBO across a spectrum of neurological conditions, including Alzheimer's disease, Parkinson's disease, psychiatric disorders such as obsessive-compulsive disorder (OCD), major depressive disorder (MDD), and anorexia, as well as chemotherapy and antibody-based treatments for GBM[22–26].

Despite these advancements, delivering large therapeutic particles (stem cells, CAR-T, liposomes, and ionizable LNPs, etc.) remains a significant challenge, requiring a delicate balance between increasing PNPs and preserving microvascular integrity[33]. The ability to successfully transport larger particles across the BBB is directly linked to the efficiency of the barrier's opening. The more reactive the MBs under specific ultrasound parameters, the more significant the BBBO will be, allowing larger particles to be delivered into the brain[56] (Fig.6).

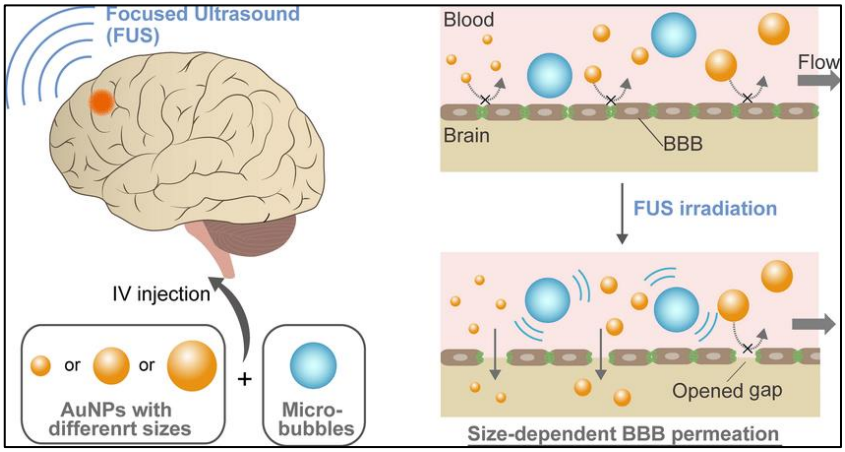

Figure 6. FUS-mediated BBBO combined with microbubbles; Particles delivery is Size-dependent: Following MB oscillations and subsequent interference with the BBB integrity, some particles will cross while for others the opened gap would be insufficient. *Illustration adopted from Ohta, Seiichi, et al.* (2020)[56].

Our lab previously demonstrated that exciting MBs at 250 kHz—a frequency an order of magnitude below their resonance (<1 MHz)—substantially enhances their oscillations compared to the MHz range[41,48,49,57,58], establishing the basis for our

hypothesis that low-frequency ultrasound facilitates the delivery of large particles, including at the size of LNPs across the BBB.

3.8. LNPs-based therapy

Optimizing mRNA delivery platforms is vital for the successful development of mRNA therapeutics[9]. RNA-based treatments represent a breakthrough in addressing previously untreatable diseases and genetic disorders by modulating disease-related gene expression. mRNA is a relatively large molecule (10^5–10^6 Da), which limits its ability to diffuse into cells. Its negative charge further complicates transport across the anionic cell membrane. Additionally, mRNA is unstable and highly susceptible to enzymatic degradation, with an average intracellular half-life of few hours only. Without an effective delivery system, synthetic mRNA has little chance of reaching the cytoplasm, where it can be translated into therapeutic proteins.

To address these challenges, various non-viral delivery systems, including liposomes and polymers, have been designed to protect and enhance the cellular uptake of mRNA therapeutics[9]. In early research, cationic lipids were incorporated in liposomes to form electrostatic interactions with the anionic mRNA. Although they allowed effective mRNA encapsulation, their cationic nature induced cellular toxicity and immunogenicity, in both in vitro and in vivo models, due to undesired interactions with critical enzymes and cellular membranes.

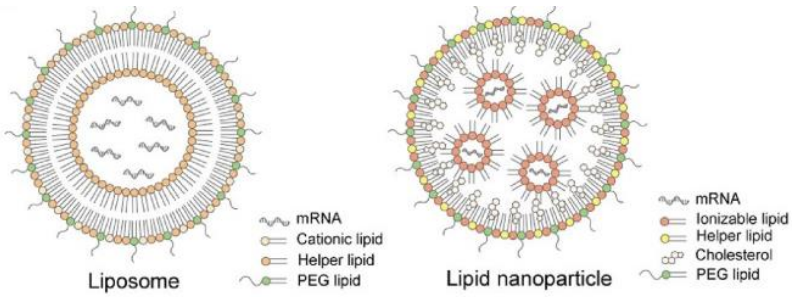

Figure 7. **Structure of cationic liposomes and Lipid Nanoparticles (LNPs).** *Illustration adopted from Jeong et al.* (2023)[9].

Then, a new generation of ionizable lipid were designed, aiming at reducing toxicity while maintaining transfection efficiency (Fig.7). Ionizable lipids are structurally similar to cationic lipids, with hydrophilic heads and hydrophobic tails, but

their key feature is the ability to change charge based on pH (Fig.8). In the relatively acidic environment used for their assembling, they carry a positive charge that allows stable binding with the anionic mRNA to form LNPs. At physiological pH of the body, the charge neutralizes, reducing toxicity and enhancing systemic circulation time. Once they are uptaken into the cells, the strong acidic conditions of endosomal compartments cause the ionizable lipids to regain their positive charge, disrupting the endosomal membrane and releasing the mRNA into the cytosol. This dynamic charge property is crucial for effective therapeutic delivery. Additionally, incorporation of cholesterol stabilizes the particles and promotes adsorption onto plasma protein ApoE and interaction with low-density lipoprotein receptor (LDLR) on the cells, leading to increased uptake through receptor-mediated endocytosis[9].

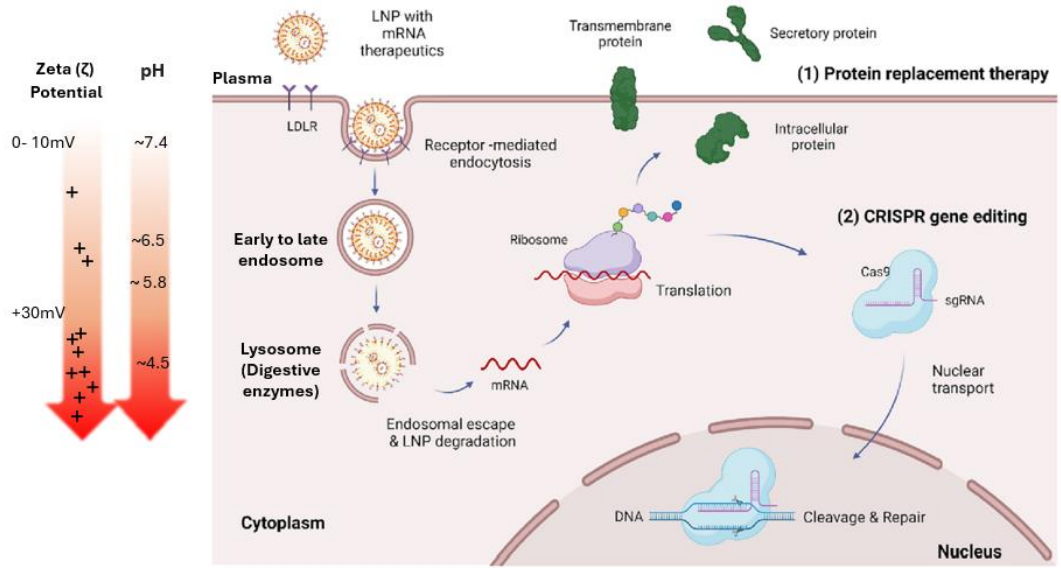

Figure 8. Mechanism of mRNA-LNPs intracellular uptake. *Illustration adapted from Jeong et al.* (2023)[9].

Consequently, LNPs represent a promising avenue for treating various pathologies through genetic manipulation. Among their advantages are enhanced target specificity, good biodegradability, heightened protein expression, increased therapeutic efficacy and manageable immunogenicity[59]. Compared with AVVs which have limited RNA capacity, LNPs can encapsulate either siRNA, long mRNA nucleic acids or even both Cas9 and sgRNA sequences within the same particle. For instance, in one study researchers were able to administrate via stereotactic injection LNPs incorporating both Cas9 and sgPLK1 within the same particle, demonstrating therapeutic effect on survival

in orthoptic GBM mouse model[13]. Lately, they had been FDA-approved for the indications of Hereditary transthyretin amyloidosis (hATTR) Onpattro® and the mRNA-based COVID-19 vaccines by Moderna and Pfizer-BioNTech[10,11].

In cancer therapy, LNPs offer a promising strategy for gene manipulation, in particularly by delivering modified messenger RNA. The suppressed immune system in cancer patients is characterized by lower T-cell counts, less effector immune cells infiltration, higher levels of exhausted effector cells and higher levels of immunosuppressive cytokines, such as TGF-β[13]. Pro-inflammatory cytokines have been shown to promote anti-tumor immune responses, inducing potent tumor regression and increasing overall survival in various tumor models[12]; however, a significant limitation of this strategy is the lack of effective and specific delivery methods, which can lead to severe adverse reactions. LNP-mediated delivery of pro-inflammatory cytokines directly to the tumor site has the potential to reduce systemic adverse reactions and improve therapeutic outcomes. Thus, certain pro-inflammatory cytokines encapsulated as mRNA-LNPs holds a great therapeutic potential by promoting peripheral T-cell expansion and antagonizing the immunosuppressive network.

While LNPs emerge as promising carriers for gene therapy, still, their application in advanced brain therapies is impeded by their limited permeability across the BBB, and previous studies utilizing LNPs to treat brain diseases often resort to direct administration into the tumor via stereotaxic injection[13]. Here, we aim to establish the use of low-frequency FUS combined with MBs for the noninvasive delivery of LNPs across the BBB and into the tumor.

3.9. Glioblastoma: disease and therapy

GBM , a WHO grade IV glioma, is the most prevalent malignant primary brain tumor, with a ~6.8% five-year survival rate[8]. GBM is considered a complex malignancy with multiple gene mutations, aberrations, and overexpression together with a high infiltration rate and resistance to apoptosis[60]. The tumor microenvironment is highly heterogeneous, and blood-brain tumor barrier varies between areas that exhibit highly permeable blood vessels, and other areas maintaining BBB-like integrity or display vascular abnormalities[7] (Fig. 9). In tumor areas where the blood-brain tumor barrier is compromised, macromolecules such as antibodies and other compounds, typically

restricted from entering the brain by efflux transporters, may extravasate and interact with glioma cells. However, in regions where the BBB remains intact, it protects isolated tumor cells from effective therapeutic delivery. This protection significantly impacts the efficacy of anti-tumor treatments, particularly as these regions are unresectable and often contribute to tumor recurrence[61].

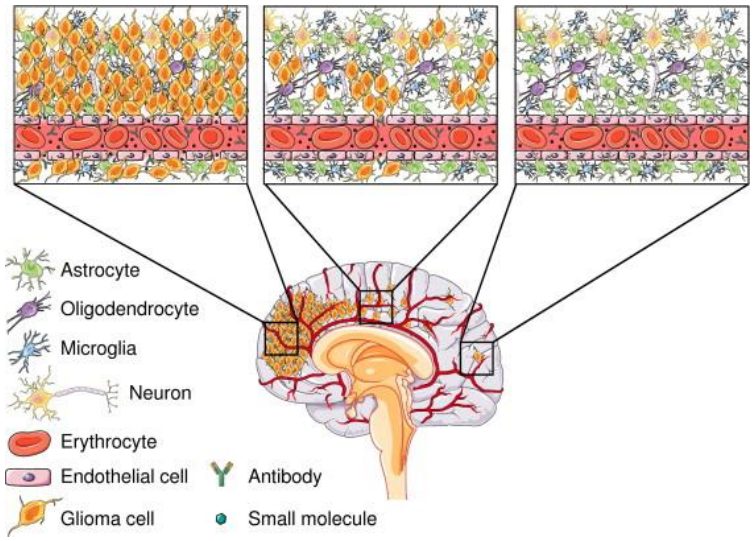

Figure 9. Varying levels of BBB integrity inside GBM tumor; The central tumor mass exhibits a significantly compromised BBB (left panel), while peripheral invasive areas show moderate leakiness (middle panel), and regions distant from the main tumor mass maintain an intact BBB (right panel). *Illustration adopted from O. van Tellingen et al.* (2015)[8].

The traditional treatment consists of tumor resection together with aggressive radiation and chemotherapy[61]. This therapeutic strategy almost has not changed since 2005, when the chemotherapy Temozolomide was approved. This therapeutic approach extended GBM patients' life expectancy to ~15 months. Although recent progress in genomics and proteomics paved the way for identifying potential therapeutic targets for treating GBM, with many clinical trials conducted in the field, the majority of these leading drug candidates remain ineffective due to the high recurrence rate and the development of drug resistance[861]. Thus, novel and effective treatments to GBM still present an unmet need.

Promoting anti-tumor immune responses by pro-inflammatory cytokines has been shown to promote potent tumor regression and increase overall survival in various tumor models. For example, IL-7 is one of the members of the IL-2 superfamily. IL-7 stimulates the proliferation of all cells in the lymphoid lineage (B cells, T cells and NK

cells). In cancer patients, the suppressed immune system is characterized by lower T cell counts, less effector immune cells infiltration, higher levels of exhausted effector cells and higher levels of immunosuppressive cytokines, such as TGF-β[62]. The expression of IL-7 holds a great therapeutic potential by promoting peripheral T cell expansion and antagonizing the immunosuppressive network. It was previously shown that IL-7 presents antitumor effects in glioma and *In vivo* administration of IL-7 resulted in decreased cancer cell growth and prolonged the survival of tumor-bearing hosts[63]. Also, it has been shown that the secretion of IL-7 from glioma cells reduced the tumorigenicity *in vivo* in proportion to the amount of IL-7 produced[64]. IL-7 as an immunotherapy agent has been examined in many pre-clinical animal studies[65–67] and more recently in human clinical trials for various malignancies[68,69].

Despite these promising results, the major limitation of this strategy is the lack of effectiveness and specific delivery approaches which can result in severe adverse reactions in humans[62,69]. The example of IL-7 highlights the potential of LNP-mediated delivery to reduce systemic adverse reactions and improve therapeutic outcomes, promoting the advancement of its use in cancer therapy. On another case, LNPs can also be used for encapsulation of other cytokines to induce an anti-inflammatory response, which is beneficial in neuro-immune diseases. For instance, in inflammatory bowel disease (IBD), the expression of the anti-inflammatory cytokine IL-10 has been shown to significantly reduce pathological symptoms, such as weight loss, colon shortening, and inflammatory infiltration, in colitis-bearing mice[59]. These contrasting examples of cytokine-based therapies - whether pro- or anti-inflammatory - highlight the versatility and therapeutic potential of mRNA-LNPs as a delivery platform, enabling tailored treatments for both brain cancer and immune-related diseases. Hence, in this thesis we focus on developing ultrasound-based technology for LNPs noninvasive brain delivery that could open new avenues for GBM therapy as well as other neurological conditions.

4. Methods and materials

4.1. Microbubble preparation

MBs composed of a phospholipid shell and a Perfluorobutane (C4F10) gas core, were prepared using the thin film hydration method as previously reported and briefly summarized here[41,70]. Two lipids of 1,2-distearoyl-sn-glycero-3-phosphocholine (DSPC; 850365C) and 1,2-distearoyl-sn-glycero-3- phosphoethanolamine-N-[methoxy (polyethylene- glycol)-2000] (ammonium salt) (DSPE-PEG2K; 880129C) (Sigma Aldrich, St Louis, MO, USA) were mixed at a molar ratio of 90:10. A buffer mixture (10% glycerol,10% propylene and 80% saline (pH 7.4) were added to the lipid film and sonicated at 62°C until full transparency. The resulting 2.5 mg/ml MB precursor solution was aliquoted into 1 ml in each vial and saturated with Perfluorobutane gas (C_4F_{10}, Cas no. 355-25-9, F2 Chemicals LTD, UK) to remove air. Upon use, the solution was activated by mechanical shaking with a VialMix shaker (Bristol-Myers Squibb Medical Imaging Inc., MA, USA) and centrifuge to purify MBs with radii smaller than 0.5 µm. Size selection was applied to remove MBs with radii larger than 5 µm. The MBs size and concentration were measured with a particle counter system (AccuSizer® FX-Nano, Particle Sizing Systems, Entegris, MA, USA) and showed median diameter of 1.5 µm and a typical concentration of ~$5x10^9$ MB/ml (Fig. 10). The MBs were used within three hours of their activation.

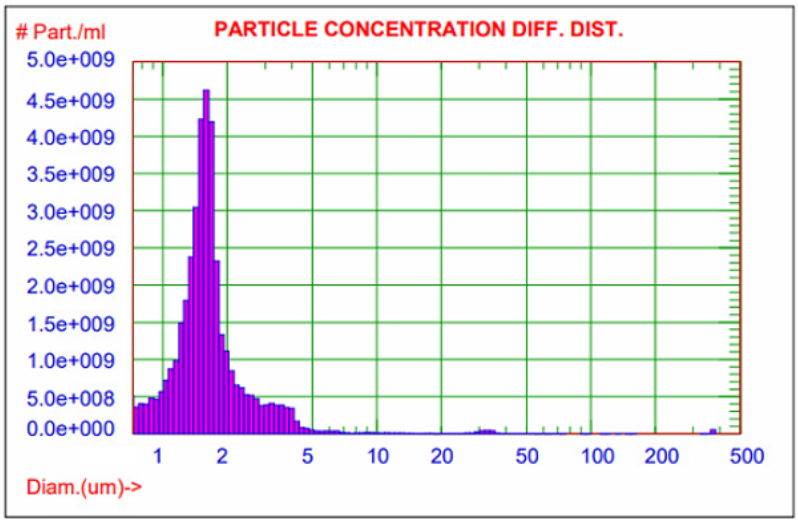

Figure 10. Microbubbles size distribution and concentration (Representative measurement using Accusizer).

4.2. RNA-LNP preparation & characterization

Tracer RNA-LNPs were prepared using a previously described method[71]. Briefly, one volume of lipid mixture (Ionizable lipid SM-102, DSPC, Cholesterol, PEG-DMG at 50:10:38.5:1.5 molar ratio) in ethanol combined with mRNA (1:6 molar ratio RNA to ionizable lipid, either 50% siRNA-Cy5 or mRNA-LUC) in a citrate buffer, pH 4.5 were injected into a NanoAssemblr microfluidic mixing device (Precision Nanosystems Inc., Canada) at a combined flow rate of 12 mL min-1. The resulting LNPs were dialyzed twice using 0.5x phosphate buffered saline (PBS) (Dulbecco's PBS w/o CA & MG) (pH 7.4) for 16 h and 4h to remove ethanol. Cholesterol, DSPC (1,2-distearoyl-sn-glycero-3-phosphocholine), polyethylene glycol (PEG)–DMG (1,2-dimyristoyl-rac-glycerol) were purchased from Avanti Polar Lipids Inc (Alabaster, AL, USA). Heptadecan-9-yl 8- ((2-hydroxyethyl)(6-oxo-6-(undecyloxy)hexyl)amino)octanoate (SM-102) was synthesized in-house as previously described57. mRNA sequences were purchased from TriLink (San Diego, CA, USA), and synthesized with complete N1-methyl-pseudouridine nucleotide substitution. siRNA-Cy5 was purchased from Integrated DNA Technologies, Inc. The resulting LNP sizes were characterized by dynamic light scattering (DLS) (Zetasizer Ultra, Malvern, Panalytical, Westborough, MA, UK). Zeta potential was determined using the Zetasizer S system (Malvern, Worcestershire, UK). Encapsulation efficiency was determined using the RiboGreen essay (Thermo Fisher Scientific, Waltham, MA, USA). Concentration and size distribution were performed on diluted samples (1:5,000 in PBS) using NanoSight (NTA, NS300, Malvern, UK).

4.3. In vitro RNA-LNPs transfection assay

4T1 epithelial metastatic cell-line was procured from ATCC[72]. The cells were cultured in RPMI 1640 (10% v/v fetal bovine serum, 1% v/v penicillin–streptomycin, and 0.292 g L−1L-glutamine) and incubated at 37 °C in a humidified 5% CO2 incubator until reaching 85-90% confluency, then collected using TrypLE Express dissociation reagent (Gibco Corp, 12604-013, Grand Island, NY, USA). The 4T1 cells were then treated with either 50% Cy5-siRNA-LNPs (165 mg/ml) at concentrations of 2 and 4 µg per 10^6 cells, or with mRNA-LUC-LNPs (250 mg/ml) at a concentration of 1 µg per 10^6 cells. The Cy5 cellular signal was evaluated between 0.5 and 6 hours after LNP

addition using fluorescence microscopy (Cy5 filter, x20) following a PBS wash. For mRNA-LUC-LNPs, cells were incubated for 24 hours, after which Luciferase expression was assessed by adding luciferin (E1910, Dual-Luciferase® Reporter Assay System, Promega) and measuring bioluminescence using a plate reader within 1 hour.

4.4. In-Vivo BBBO Experiments

FUS setup

The FUS setup was composed of spherically focused single-element transducer (H115, Sonic Concepts, Bothell, WA, USA) that was located at the bottom of a water tank facing upwards (Fig. 11C), operated by a transducer power output system (TPO-200, Sonic Concepts) (Fig. 11B). The transducer had a diameter of 64 mm and a focal distance of 45 mm. It supported center frequencies of 80, 250, and 850 kHz via custom matching networks (purchased from Sonic Concept). The PNPs for each center frequency were calibrated using a needle hydrophone (NH0500, Precision Acoustics, UK). For the in vivo experiments, the mice were positioned in the setup on top of an agarose spacer (Fig. 11A). This spacer was prepared by dissolving agarose powder (A10752, Alfa Aesar, MA, USA) in distilled water to achieve a 1.5% concentration, followed by heating to completely dissolve the agar powder and remove gas bubbles. The solution was poured into a mold of 5 cm x 5 cm x 1 cm (length x width x height) and cooled at room temperature. The spacer was placed on top of the water tank as a mouse bed. A black head holder was constructed on the upper plate, aiding in securing the mouse's head at the FUS focal spot, while continuously providing anesthesia[73]. To precisely target the RH, the setup was equipped with a vertically fixed laser pointer to co-align with the transducer’s focal spot (Fig. 11D).

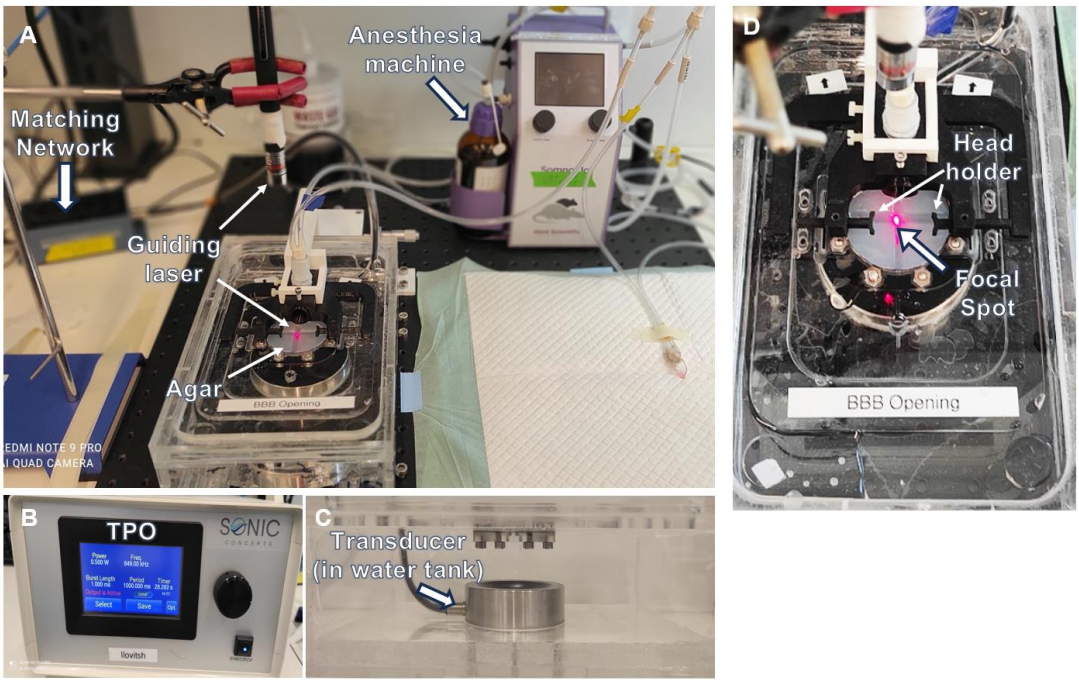

Figure 11. Experimental ultrasound setup. (A) Top view of the setup including: a matching network, an anesthesia machine, and a single-element transducer positioned at the bottom of a water tank. An agar pad is serving as a mouse bed and placed on top of the water tank. (B) TPO. (C) A side view of the transducer at the bottom of the water tank. (D) Head holder located above the agarose pad is used to position the mouse's head and supply anesthesia, while the guiding laser indicating the transducer's focal spot on the surface of the agar pad.

Animal preparation

Eight to twelve-week-old female C57BL/j6 mice, weighing between 19-23 grams (Harlan, Jerusalem, Israel), were used for the in-vivo FUS-mediated BBBO experiments. All animal procedures were approved by the Institutional Animal Ethics Committee at Tel-Aviv University and carried out in accordance with guidelines.

Mice preparation for the BBBO procedure was as follows: all mice were anesthetized with 2% isoflurane using a low-flow vaporizer system (120 ml/min, SomnoFlo, Kent Scientific, Connecticut, USA). Their heads were fully shaved with a machine, and any remaining hair was removed using hair removal cream (Veet, Reckitt Benckiser, France), that was applied for 40 seconds and then removed with a water-soaked pad. The region of interest in the RH was marked by a dot with a marker to assist in the positioning of the mice.

BBBO procedure

Mice were systemically injected with 2 x 107 MBs per 20 gram of body weight, in 50 µl of degassed PBS (Dulbecco's PBS w/o CA & MG). US gel was applied on top of the agarose spacer, and the mouse's head was positioned supine on top of the gel. The FUS treatment was operated within 60 seconds from MBs injection in varied parameters depending on the tested center-frequency. FUS treatments in 850 kHz center-frequency comprised of 1 ms bursts and RPF of 1 Hz (duty cycle of 0.1%), testing nine PNPs: 500, 400, 350, 300, 275, 250, 200, 150, 125 (n=17 in total). In 80 kHz center-frequency, 3.25 ms bursts and RPF of 1 Hz were operated (duty cycle of 0.1%) and the tested PNPs were: 180, 120, 90, 75 (n=8). The PNPs were optimized for 850 kHz and 80 kHz, by gradually decreasing the PNP until safe BBBO was observed, without signs of microhemorrhage in histology. For 250 kHz, the PNP was set at 200 kPa with the same PRF (1Hz) based on previous optimization[58]. Immediately after the FUS treatment, mice were systemically injected with one out of six different molecules as described next:

- **EB delivery:** EB (E2129, Sigma Aldrich) dye solution of 2% in PBS at 4 ml/kg and was systemically injected and allowed to circulate for a duration of 28 minutes before mice were sacrificed. This time point was selected based on previous research[58]. Once identified, the optimized BBBO parameters (850 kHz, 125 kPa, 1 ms bursts, duty cycle of 0.1%) were used in all subsequent experiments.
- **Dextrans delivery:** For experiments with dextran molecules, three distinct molecular weights (4 kDa, 70 kDa, and 150 kDa), each labeled with a fluorescent moiety were used (Antonia Red-lysine-dextran [ARLD4, ARLD70], TdB Labs AB, Uppsala, Sweden, and 150 kDa FITC-Dextran [68042-46-8], Sigma-Aldrich). To maintain consistency, each dextran dose was 1 mg in 100µl and circulation time was 10 minutes before scarification34,58,59. Mice were divided into three groups (n=5 in each): treated group injected with 1 mg of red-labeled 70 kDa dextran; a second treated group injected with a mixture of red-labeled 4 kDa and green-labeled 150 kDa dextrans, and a control group injected with a mixture of all three dextrans.
- **LNPs delivery:** For experiments with LNPs, two types of LNPs were fabricated composing of either 50% siRNA-Cy5 or mRNA-LUC. For siRNA-Cy5-LNP, a

fixed dose of 1mg/kg was systemically injected, and brains were harvested 2.5 hours post-treatment. A total of 15 (n=3 each) mice were divided into four groups treated at descending pressures (300, 250, 150, 125 kPa) and NTC. In the case of mRNA-LUC-LNP, a fixed dose of 1mg/kg dose was systemically injected, and mice were imaged 24 hours post BBBO. A total of 21 mice, all injected with mRNA-LUC, were divided into four groups: LNPs only (n=6), MBs + LNPs (n=3), FUS + LNPs (n=4), and MBs + FUS (125-135 kPa) + LNPs (n=8). 24 hours post treatment, prior to the IVIS imaging the mice were injected intraperitoneally with XenoLight d-luciferin (15 mg/kg) (122799, PerkinElmer Inc.)14. Post-sacrifice, brains and livers were extracted and imaged for LUC signal. The bioluminescence analysis was performed using the Living Image software comparing the samples total flux [p/s].

At the end point of each experiment) EB / Dextrans / LNPs), the brains were collected and positioned on top of a Tragacanth Gum paste, which had been prepared by mixing Tragacanth Gum powder (G1128-100G, Sigma-Aldrich) in distilled water at a concentration of 15% (w/v). Subsequently, the samples were flashed-frozen in 2-methylbutane (Sigma-Aldrich) using liquid nitrogen and stored in a -80ºC refrigerator until cryo-sectioning to 20 µm slices.

4.5. GBM 005 orthotopic model

Mouse-derived glioma cell line (GBM 005, GFP+, LUC+), a gift from Prof. Dinorah Friedman-Morvinski, were established using lentiviral transduction of H-Ras and activated Akt in Cre-GFAP/p53+/− C57BL/6 mice, as previously described[74]. Maintained in stem cell medium, specifically DMEM/F:12 medium supplemented with 1% Glutamax (100X), 1% penicillin-streptomycin, B27 supplement (Invitrogen), N2 supplement (Invitrogen), heparin (50 µg/mL), EGF (20 ng/mL), and FGF2 (20 ng/mL), the GBM 005 cells were cultured as spheres and split every 3-4 days using TrypLE Express dissociation reagent (Gibco Corp, 12604-013, Grand Island, NY, USA) when reaching 90% confluency. A total of 30 eight-week-old female C57BL/6JOlaHsd mice (Envigo, Jerusalem, Israel) were anesthetized using isoflurane, positioned in the Kopf Stereotaxic Alignment System, and inoculated with 3×105 GBM 005-GFP-luciferase cells in a 1.5-µl volume using automatic syringe pump in a rate of 0.3 µl/min. Injections were made to the right frontal lobe: ~1.5 mm lateral, 2 mm caudal from bregma, and at

a depth of 2.3 mm. Tumor inoculation and growth monitoring was performed by bioluminescence imaging (IVIS Spectrum, PerkinElmer Inc.) every 5 days post tumor cell implantation until the experiment between days 17-21. XenoLight d-luciferin was injected at 15 mg/kg intraperitoneally and mice were imaged within 10 to 30 mins post injection. Bioluminescence analysis was conducted using the Living Image software (PerkinElmer Inc.) comparing the subject's total flux[13].

4.6. Microscopy imaging and Quantitative analysis

Frozen brains were cryo-sectioned to 20-µm-thick coronal in a -20º C cryostat microtome (CM1950, Leica Biosystems). The sections were placed on standard microscope slides and kept in a slide box at -20º C until use. Upon imaging, the brain slides were thawed to room temperature and imaged within 1 hour to avoid dye diffusion. All full brain images in this study were obtained using a hybrid automated microscope (Revolution, Echo, San Diego, USA). The imaging process involved stitching 20 x 30 tiles, each measuring 0.432 mm x 0.36 mm, to create a full slice scan. These scans were conducted at 20x optical magnification. For fluorescent images the following excitation wavelengths and exposure times were used: DAPI (365 nm, 90 ms), GFP (410 nm, 460 ms), Cy5 (690 nm, 790 ms), and EB (690 nm, 90 ms). Confocal microscopy images were acquired with confocal microscope (IX-83, Olympus) using UPLXAPO x40 objective (NA 0.95) in z-stacks (1 um each, 8 stacks). The nucleus was labeled with DAPI (405 nm), GBM 005 were +GFP positive (488 nm), siRNA-LNP were labeled with Cy5 (640 nm), and subsequently merged using ImageJ® software (Fig. 22C).

Measurement of width of opening and the full brain distances in X-axis and Z-axis were conducted using the microscope software (Figs. 16B, 17B and 19C). Segmentation of the opening area with EB as a function of pressure in the representation of an ellipsoid was calculated using an ellipse function in MATLAB (version 2018a, MathWorks, Natick, MA, USA) (Fig. 16C). The values were normalized to average mouse brain size. Quantification of opening size area, microhemorrhages and markers intensity were conducted using ImageJ® software (National Institutes of Health, Bethesda, MD). Full-brain fluorescence microscopy images were first imported into ImageJ. The area of opening in red or green channel and the total brain area were manually selected. Markers' intensity was calculated by selecting an opening area at the

same size across all brain images (Fig. 17C, 19D, 22B). Quantification of BBBO-induced hemorrhage was conducted on full-brain brightfield microscopy images (without H&E staining) using the IHC toolbox in ImageJ. To reduce background noise, each hemorrhage center was defined as 200 pixels^2, and the IHC toolbox was trained to recognize relevant shades of brown from total brain area (Fig. 16G, 18).

4.7. Histology

Hematoxylin & Eosin staining; The safety of the BBBO treatments was assessed by a standard Hematoxylin (Leica 3801542) and Eosin (Leica 3801602) (H&E) staining of the 20-µm-thick frozen brain sections and scan x20 using the brightfield channel (Fig. 16E-F). DAPI Staining; Tissue slices were mounted onto glass slides and coverslipped after the application of three drops of Mounting Medium with DAPI (Fluoroshield, ab104139, Abcam). The slides were allowed to develop for 15 minutes before further analysis. Anti-Luciferase antibodies staining; Anti-Luciferase antibody staining was established to confirm LNPs' successful brain delivery and luciferase expression (Fig. 21D). Using Abcam antibodies (Anti-Firefly Luciferase, AB-ab21176 and Goat Anti-Rabbit IgG H&L, Alexa Fluor® 594), both diluted as per recommendations, 15 µm frozen brain sections were fixed in -20ºC acetone, air-dried, and permeabilized with TBS (PBS + 0.1% Triton). After a 2-hour room temperature block with 10% normal goat serum and 1% BSA in TBA, the primary antibody (1/200) was added and left overnight at 4°C. Following washes, secondary antibodies (1/500) in 1% BSA were applied for 1 hour at room temperature. The process concluded with the addition of a mounting medium with DAPI (Abcam, ab104139).

4.8. Statistical analysis

Prism 10.1.2 (GraphPad Software) was employed for the statistical analysis. A two-sided Student’s t-test was utilized to compare two experimental groups. In experiments involving multiple groups, differences among multiple populations and sub-populations were assessed using One-Way and Two-Way ANOVA with Tukey’s multiple comparisons. A value of $p \leq 0.05$ was considered statistically significant. Differences are presented on graphs in the following abbreviations: blank. for not significant, * for $p \leq 0.05$, ** for $p \leq 0.01$, *** for $p \leq 0.001$, and **** for $p \leq 0.0001$.

5. Results

5.1. LNP characterization and in-vitro transfection

Two types of LNPs were designed using the benchmark ionizable lipid sm-102 to achieve stable encapsulation of the RNA cargo, as illustrated hereby (Fig. 12).

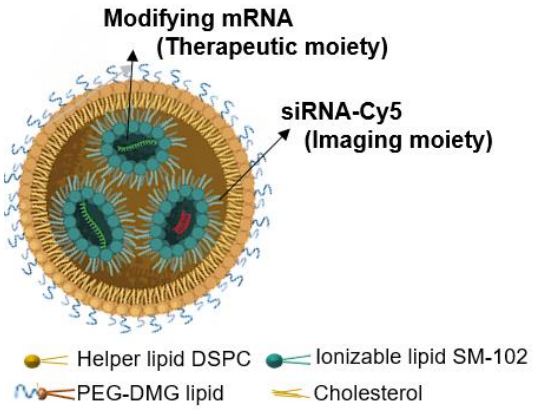

Figure 12. Illustration of ionizable LNPs: structure and cargo.

The first type of LNPs were non-coding siRNA-LNP conjugated to Cy5 ('siRNA-LNP-Cy5'), to enable the tracing of cellular uptake via fluorescent microscopy. These particles were produced at an average size of ~70 nm, with a zeta potential of -0.426mV, and their measured concentration was 4.06 $x10^8$ particles/ml. The second type were LNPs containing mRNA-luciferase sequence encoding for the luciferase protein ('mRNA-LUC-LNP'). These LNPs were produced at an average size of ~100 nm, with a zeta potential of -0.142mV, and their concentration was 3.64 $x10^8$ particles/ml (Fig. 13). They aimed at facilitating the expression of the luciferase protein and enable the bioluminescent detection of cells that were successfully transfected with the particles. Both LNPs had an encapsulation efficiency of above 95%.

For preliminary testing, LNPs cellular uptake was measured by incubating 4T1 cells with either, Cy5-siRNA-LNPs or mRNA-LUC-LNPs. Fluorescence microscopy revealed Cy5 cellular signal between 2.5 and 6 hours post-LNP addition (Fig. 14A). Additionally, cells incubated with mRNA-LUC-LNPs exhibited a significantly increased bioluminescence signal after one hour, compared to cells in the absence of LNP (Fig. 14B).

siRNA-Cy5-LNPs

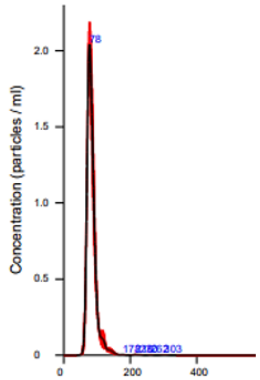

Mean:	84.0 +/- 0.2 nm
Mode:	77.9 +/- 1.1 nm
SD:	17.3 +/- 1.2 nm
D10:	69.6 +/- 0.5 nm
D50:	80.6 +/- 0.6 nm
D90:	100.5 +/- 2.4 nm
Concentration (Upgrade):	5.03e+08 +/- 4.99e+07 particles/ml

mRNA-LUC-LNPs

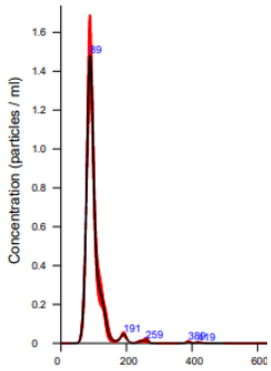

Mean:	100.5 nm
Mode:	88.9 nm
SD:	34.7 nm
D10:	77.2 nm
D50:	92.5 nm
D90:	127.1 nm
Concentration (Upgrade):	4.80e+08 +/- 1.29e+07 particles/ml

siRNA-Cy5-LNPs:

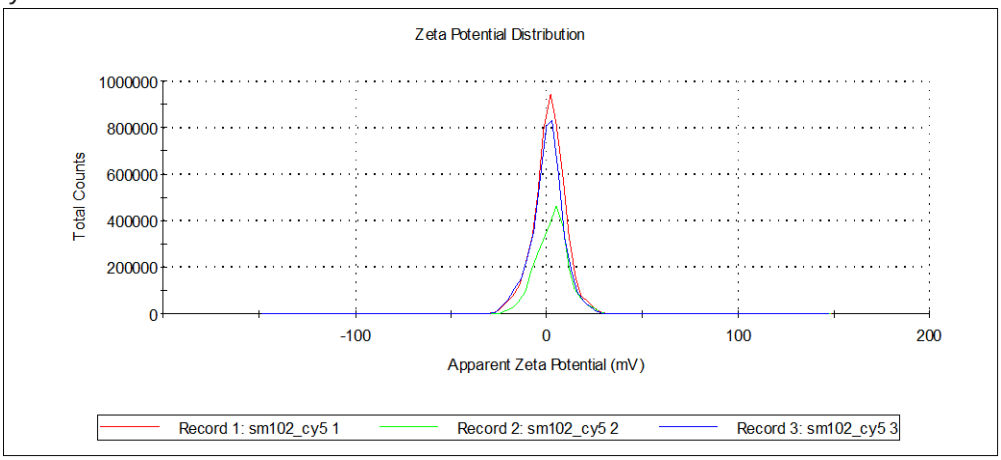

mRNA-LUC-LNPs:

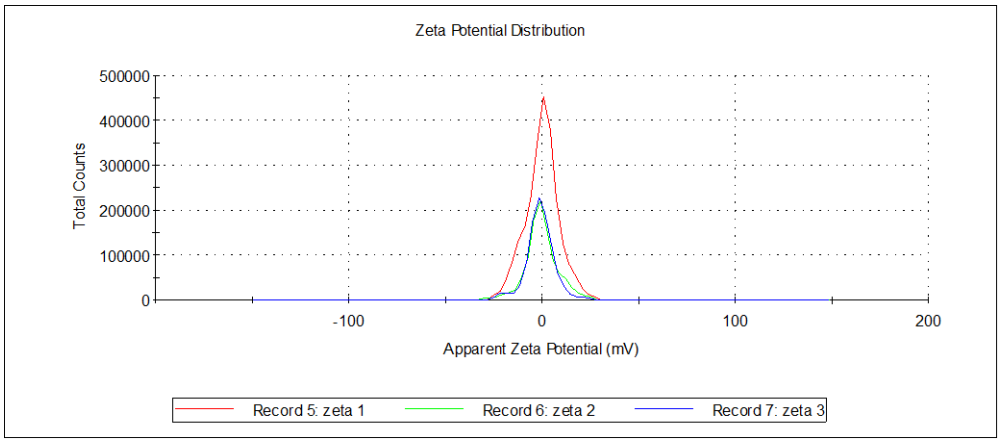

Figure 13. Representative measurements of size distribution and concentration of siRNA-Cy5-LNPs and mRNA-LUC-LNPs using NanoSight (samples are diluted 1:5,000 in PBS) and Zeta potential using Zetasizer.

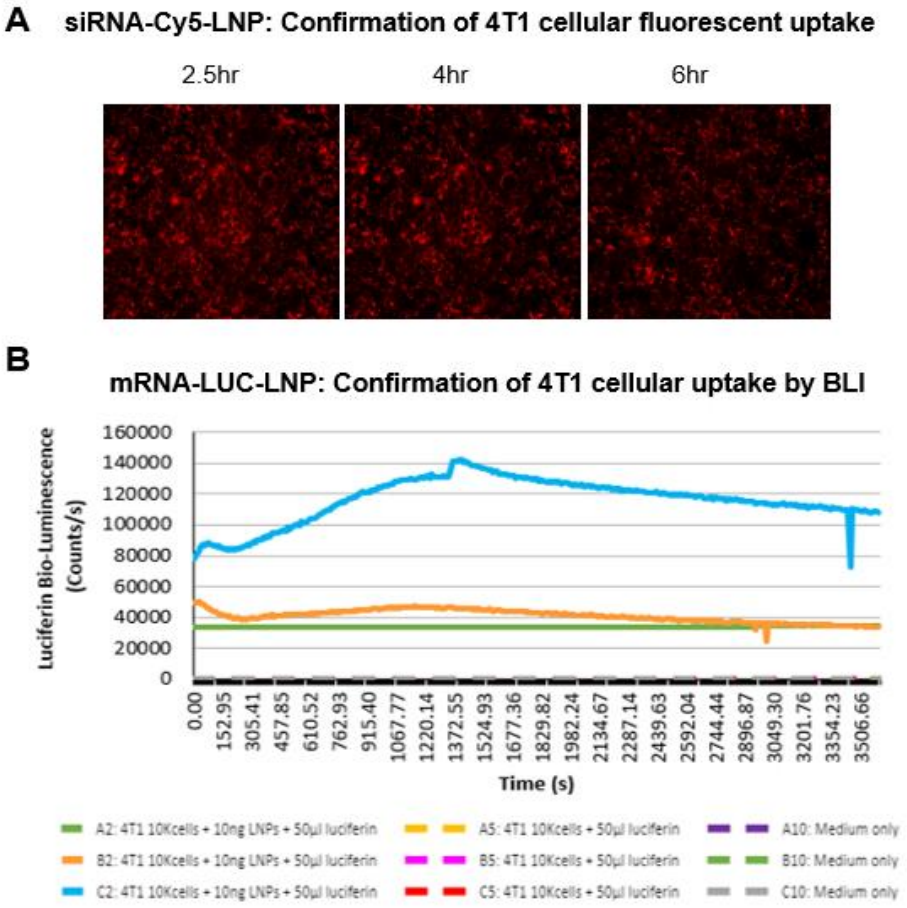

Figure 14. LNPs evaluation of in-vitro transfection. (A) siRNA-Cy5-LNP confirmation of 4T1 cellular uptake at different time points using fluorescence imaging, showing similar cellular uptake in 4T1 2.5-6 hours post incubation. (B) mRNA-luc-LNP confirmation of 4T1 cellular uptake by bioluminescence imaging (BLI). Bioluminescence signal 1 hour after: 4T1 cells incubation with sm102-mRNA-LUC-LNPs (A2-C2), 4T1 cells in the absence of sm102-mRNA-LUC-LNPs (A5-C5) or in medium only.

5.2. Low-Frequency mediated BBBO in healthy mice

5.2.1. FUS center-frequency optimization and selection

In vivo experiments were conducted using a custom setup, where the mouse was positioned supine, and a laser indicator was used to aid in targeting the right hemisphere (RH) (Fig. 15A). Initial experiments were aimed at determining the optimal center-frequency by monitoring EB extravasation patterns at 850, 250, and 80 kHz in healthy mice brains. For each center-frequency, the initial PNPs were selected based on our previous simulation results of the safe range of PNPs[48,57,58]. Among the tested frequencies, the 850 kHz center-frequency emerged as optimal for targeted BBBO in

the RH, covering an area of ~3.5 x 7 mm^2 (Fig. 15B,E). The 250 kHz center-frequency[57,58] resulted in a heterogeneous pattern concentrated only at the brain's edges (Fig. 15C,F). The 80 kHz center-frequency resulted in a strong, wide focal opening spot, but also caused microhemorrhage at 90 kPa, and only a very mild opening at 75 kPa (Fig. 15D,G,H). Based on these observations, the 850 kHz center-frequency was found optimal in mice brains and selected for further in vivo experiments aimed at the delivery of larger fluorescent particles.

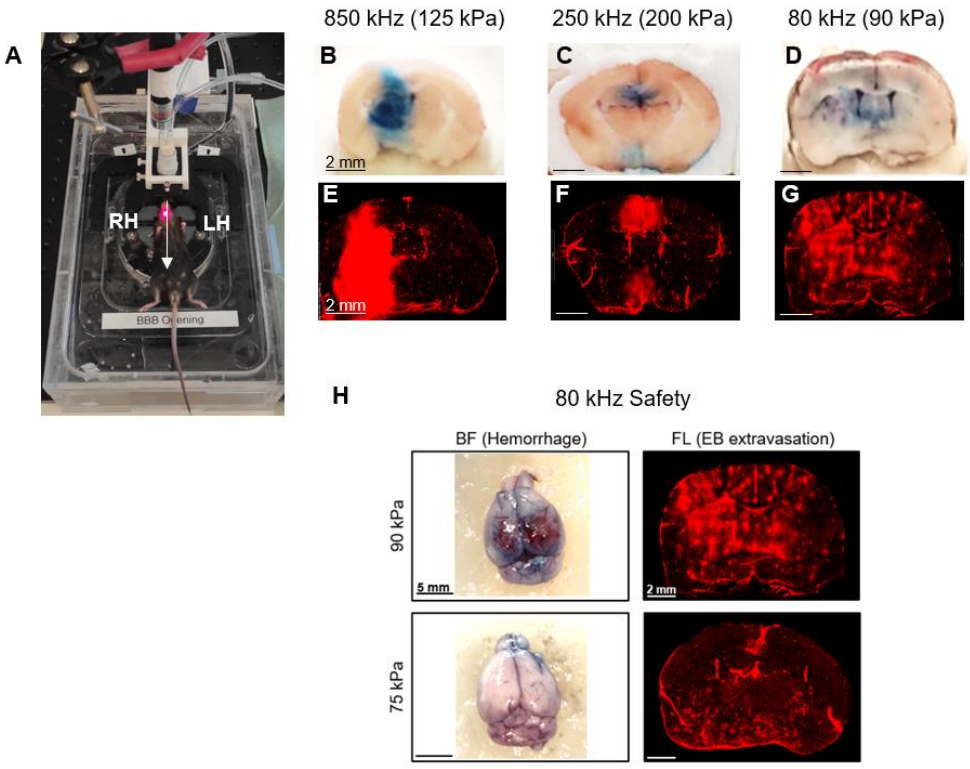

Figure 15. EB extravasation following FUS-mediated BBBO as a function of center-frequency. (A) In-vivo FUS setup that includes a fixed-laser pointer to target the RH. (B)-(G) Evaluation of BBBO at three center-frequencies: Images of EB extravasation in brains treated with a center frequency of (B) 850 kHz, (C), 250 kHz, (D) 80 kHz. (E)-(G) Fluorescence images of the brain slices from (B)-(D). (H) Representative images of safety in 80 kHz center-frequency: hemorrhage in BF at 90 kPa and respective EB signal, compared to mild extravasation in 75 kPa without damage in BF. EB extravasation was detected in the red channel. FL images were acquired with 20x objective lens. Scale bar: 2 mm.

5.2.2. FUS-mediated BBBO in 850 kHz

5.2.2.1. EB monitoring

After identifying the center frequency of 850 kHz, optimization experiments for assessing the safe range of PNPs and extravasation assessment were performed. The PNPs were progressively decreased from 500 to 125 kPa until a safe BBBO was achieved, with no microhemorrhage observed in histological analysis. BBBO was visible in the brains' RH via prone and coronal cuts (Fig. 16A). To compare the size of the BBBO as a function of PNP, the width and height of the opening along the X and Z axes were measured out of the fluorescence images of the coronal brain slices (Fig. 16B, D).

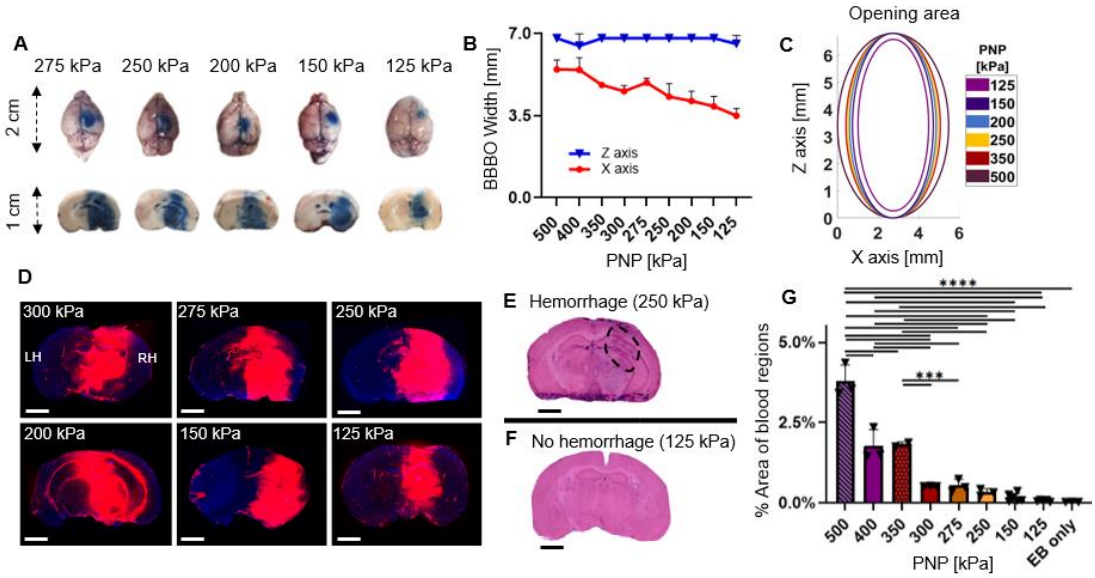

Figure 16. EB extravasation as a function of the PNP at a center-frequency of 850 kHz. (A) EB extravasation in extracted brains positioned prone and in coronal cuts. (B) Comparison of opening width and height [mm] in X and Z axis as a function of PNP. (C) Ellipsoid representation of the opening area, as a function of pressure. (D) EB extravasation imaged using fluorescent microcopy (EB/DAPI Merge). Full brain images were captured in 20x magnification and used to quantify the size of opening. Scale bar: 2 mm. (E-F) Comparison of histological evaluation of microhemorrhages (in H&E staining) at (E) 250 and (F) 125 kPa. (G) Quantification of blood presented in brain slices as a metric to evaluate microhemorrhage area out of the total brain area (%). (G) One-way ANOVA with Tukey's multiple comparison (*** for $p \leq 0.001$, **** for $p \leq 0.0001$).

Results showed a consistent opening along the Z axis with an average of 6.74 ± 0.13 mm, independent of the applied PNP (not significant), while a significant gradual decrease was observed along the X axis as the PNP decreased from 500 kPa to 125 kPa (5.46 mm ± 0.39 vs 3.49 mm ± 0.29, **** $p \leq 0.0001$; One-way ANOVA with Tukey's multiple comparison). Alternatively, these empirical results can be plotted as an ellipsoid representing the BBBO in each axis as a function of the PNP (Fig. 16C). Histological assessment of the presence of blood in each brain section as a function of PNP calculated as percent out of total brain area was used as a measure to evaluate microhemorrhage following treatment, with the amount of blood in control (EB only) sections serving as a reference to healthy brain. Presence of blood in brain histology sections decreased as a function of PNP. At 125 kPa, the values were similar to those of the control, indicating an absence of microhemorrhage and the safety of treatment at this PNP (not significant, One-way ANOVA with Tukey's multiple comparison) (Fig. 16E-G). Therefore, a PNP of 125 kPa was chosen for the following experiments.

5.2.2.2. Fluorescence dextrans delivery

After successfully delivering EB (<1 kDa), we used the same FUS parameters to study the delivery of larger dextrans with sizes of 4, 70, and 150 kDa (Fig. 17). The 4 and 70 kDa were Antonia-Red Dextran, which fluoresces in red, while 150 kDa was FITC-Dextran that fluoresces in green (Fig. 17A). Brain slices were imaged using a fluorescent microscope, where the opening size and fluorescence intensity were quantified. The width of opening in Z axis was found to be consistent across all particles: EB, 4 kDa, 150 kDa and siRNA-Cy5-LNP (not significant), with the exception of reduced height with 70 kDa compared to EB (**** for $p \leq 0.0001$; One-way ANOVA with Tukey's multiple comparison) (values were: 6.55 ± 0.36, 6.30 ± 0.31, 6.38 ± 0.33, 6.17 ± 0.35 and 5.6 ± 0.54, respectively). In the X axis, opening with EB (3.49 ± 0.30) was similar to 70 kDa (3.52 ± 0.15), and stronger than 4 and 150 that overlapped (3.05 ± 0.16) (*** for $p \leq 0.001$; One-way ANOVA with Tukey's multiple comparison) (Fig. 17B).

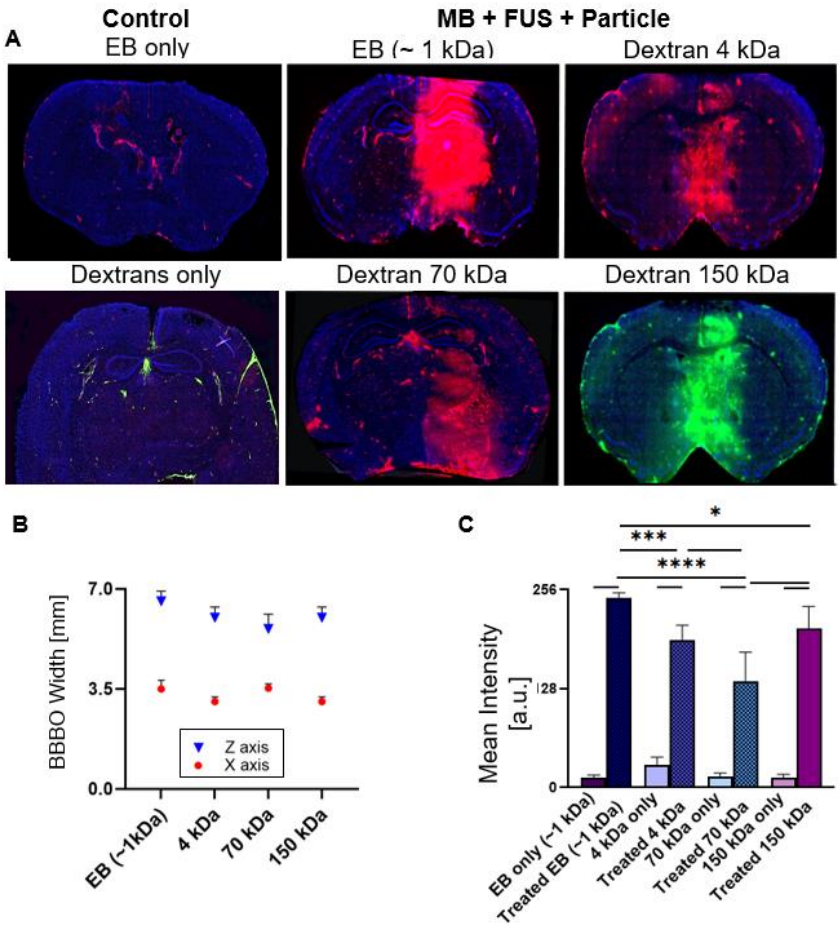

Figure 17. Delivery of EB and 4-150 kDa fluorescent dextran. (A) Fluorescence microcopy images (EB/DAPI Merge) of brain slices following BBBO showing delivery of: left column: controls of EB only, Dextrans only (mix of all three dextrans: 4,70 and 150 kDa), middle and right columns: Treated brains with MB+FUS and: EB (~ 1 kDa), 4 kDa Dextran Antonia Red, 70 kDa Dextran Antonia Red and 150 kDa Dextran FITC. Images were captured in 20x magnification. Scale bar: 2 mm. (B) Size of the opening in the X and Z axes as a function of delivered particle. (C) Fluorescence marker's intensity comparison between the different molecules and their controls (* for $p \leq 0.05$, *** for $p \leq 0.001$, **** for $p \leq 0.0001$.; Two-Way ANOVA with Tukey's multiple comparison).

Comparative analysis (Two-Way ANOVA with Tukey's multiple comparison) of fluorescence intensity in the BBBO area compared to control revealed that EB exhibited the strongest intensity among the particles that were tested (Fig. 17C). 4 and 150 kDa dextran presented a similar intensity (not significant), and a stronger intensity over 70 kDa dextran (*** $p \leq 0.001$) (with values of: EB: 245.73 ± 6.53 a.u., Dextran 150 kDa: 204.78 ± 28.04 a.u, Dextran 4 kDa: 190.5 ± 19.06 a.u. and Dextran 70 kDa: 133.72 ±

37.1 a.u.). In each group, treated brains exhibited significantly higher marker intensity compared to their control counterparts (**** $p \leq 0.0001$) (from left to right: EB: 245.73 ± 6.53 a.u. vs. 13.48 ± 2.38, Dextran 150 kDa: 204.78 ± 28.04 a.u. vs 12.52 ± 4.13, Dextran 4 kDa: 190.5 ± 19.06 a.u. vs 27.42 ± 10.18 and Dextran 70 kDa: 133.72 ± 37.1 a.u. vs 13.65 ± 4.66 a.u.). Notably, the 4 kDa Dextran also showed a diffusion pattern towards the lateral parts of the brain slices, in contrast to the more localized EB distribution represented, however differences were not significant.

5.2.2.3. RNA-based LNP delivery in healthy brains at 850 kHz

siRNA-Cy5-LNP

The first type of LNP that was used was a non-coding siRNA-LNP conjugated to Cy5 that was used as a marker to quantify the brain delivery via fluorescent microscopy. Since these particles are significantly larger than the dextrans, we started with a higher PNP of 300 kPa and gradually lowered it to the minimum pressure at which a clear opening was achieved without microhemorrhage (Fig. 19). At the highest PNP of 300 kPa, the opening was accompanied by microhemorrhage, but at 125 kPa, which is the PNP we also used for the dextran delivery, we achieved particle delivery with similar fluorescence intensity to that of the higher PNP, but without histological damage and full recovery of mice (Fig. 18).

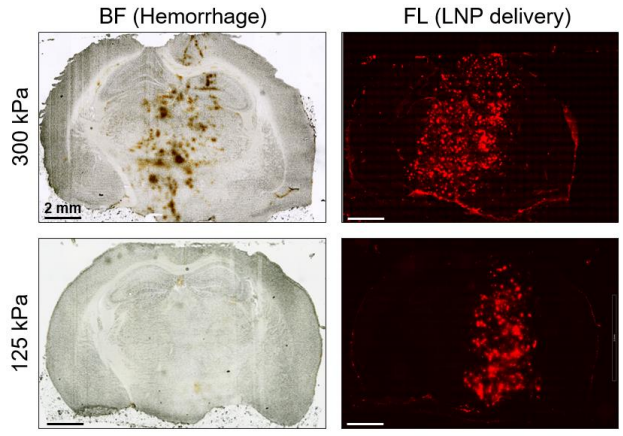

Figure 18. Safety evaluation of siRNA-Cy5-LNP delivery in 850 kHz: hemorrhage in BF at 300 kPa and respective siRNA-Cy5-LNPs signal in fluorescent microscopy (in the Red channel), compared to reduced delivery of the LNPs in 125 kPa without a damage in BF. Scale bar: 2 mm (magnification: x20).

First, a comparative analysis of the mean intensity revealed similar fluorescence signal in the BBBO region for all of the PNPs that were tested (not significant), with a significantly increased intensity compared to LNP only control (Fig. 19B) (** $p \leq 0.01$, **** $p \leq 0.0001$; One-Way ANOVA with Tukey's multiple comparison). When calculating the opening width in the X axis, measurements were: 4.03 ± 0.42 at 300 kPa, 3.428 ± 0.245 at 150 kPa, and 3.25 ± 0.11 at 125 kPa (Fig. 19C). Importantly, reducing the pressure until 125 kPa did not compromise particles delivery (not significant), and at the same time achieved increased safety with no clinical or histological damage. At the same pressure of 125 kPa, we successfully delivered a variety of particles of different sizes to the brain (Fig. 17C, 19D). A direct comparison of all the particles indicates that EB has the highest fluorescence intensity, with the delivery being 18.2 times that of its control. Following that, 150 kDa with a 16.4-fold, siRNA-Cy5-LNP with a 10-fold, 70 kDa with a 9.8-fold and 4 kDa dextran with a 7-fold increase in signal (Fig. 19E) (* $p \leq 0.05$; One-Way ANOVA with Tukey's multiple comparison).

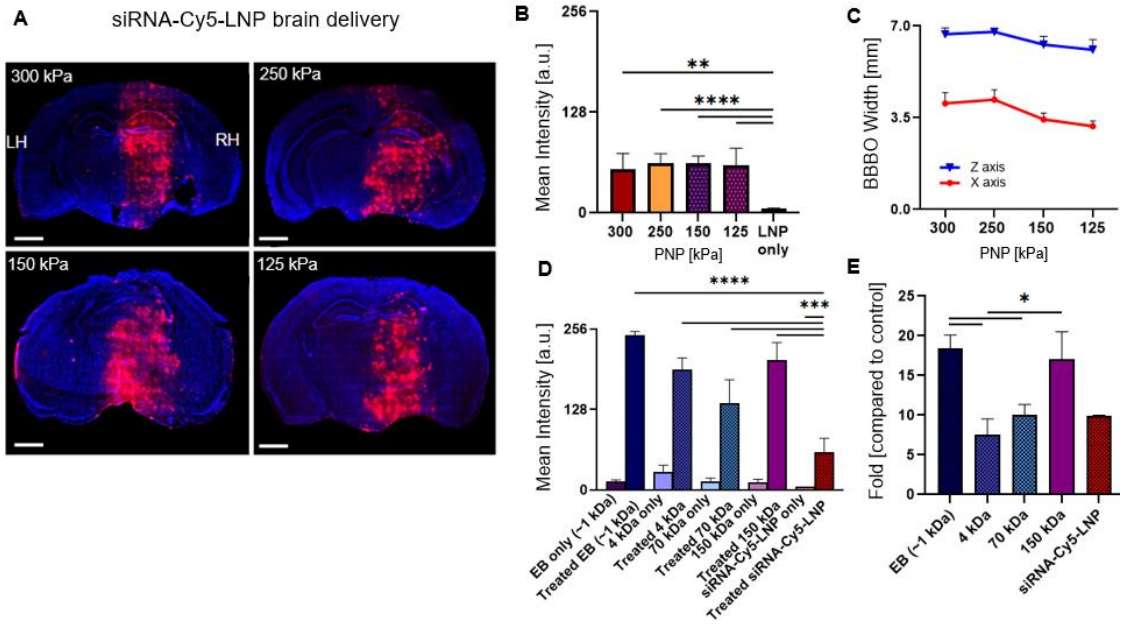

Figure 19. siRNA-Cy5-LNPs brain delivery in healthy mice in 850 kHz. (A) Fluorescence microcopy images of brain slices after BBBO showing delivery of siRNA-Cy5-LNP (~70 nm) as a function of PNP. Images were captured at a 20x magnification. Scale bar: 2 mm. (B) Comparison of siRNA-Cy5-LNP mean intensity in the BBBO region as a function of the PNP (** $p \leq 0.01$, **** $p \leq 0.0001$; One-Way ANOVA with Tukey's multiple comparison). (C) Size of the opening in the X and Z axes as a function of the PNP. (D) Comparative analysis of all

BBBO delivery of 1,4,70,150 kDa particles and siRNA-Cy5-LNP (~70 nm) and their controls. (E) The graph in (D) presented as the fold increase in intensity compared to the controls (* $p \leq 0.05$; One-Way ANOVA with Tukey's multiple comparison).

mRNA-LUC-LNP

After successfully delivering the fluorescent siRNA-Cy5-LNPs, LNPs containing mRNA and luciferase were fabricated by encapsulation of mRNA-luciferase sequence stabilized with sm-102, with a mean diameter of 100 nm (illustrated in Fig. 12, Fig. 13). These particles are bioluminescent and enable the imaging of the LNPs in the whole brain. Luciferase expression was evaluated using bioluminescence imaging (IVIS) to measure the total flux in whole brains and livers, 24 hours post FUS+MB+LNP treatment (Fig. 20A). The brains total flux in the group of MB + FUS + LNP versus the three control groups (FUS + LNP, MB + LNP, and LNP only) indicated a significant improvement in the total flux (** $p \leq 0.01$; One-way ANOVA with Tukey's multiple comparison), with a 12-fold increase compared to the LNP-only group (Fig. 20B). Livers were used as positive control for the mRNA-LUC-LNP injections, showing no significant difference between the different groups (Fig. 20C). These results further support the successful delivery of LNPs into cells, facilitating luciferase protein expression in the transfected brain cells.

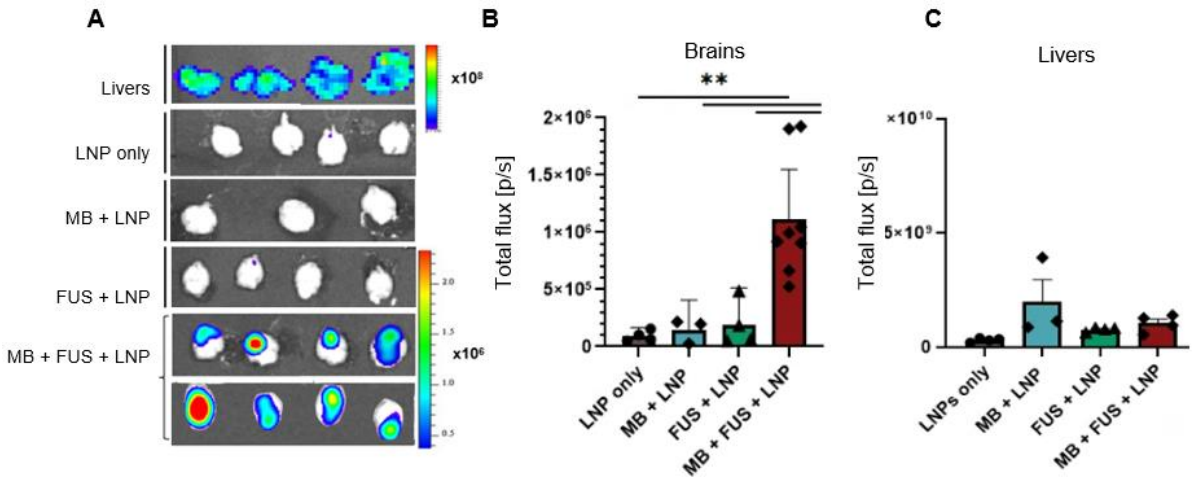

Figure 20. mRNA-luc-LNPs brain delivery in healthy mice. (A) Bioluminescence images of livers and whole brains mRNA-LUC-LNP expression 24 hours post BBBO. (B-C) Comparison of total flux for the treated group (MB + FUS + LNP) vs controls (FUS + LNP, MB + LNP, and LNP only) in brains (B) and livers (C). (B-C) One-way ANOVA with Tukey's multiple comparison, ** for $p \leq 0.01$).

5.2.3. 250 vs. 850 kHz center-frequency

Compiling with our previous interest in evaluation of 250 kHz center-frequency for FUS-mediated BBBO, we decided to conduct another experiment to check the delivery and expression 24 hours post treatment of mRNA-LUC-LNP in this lower center-frequency. The treated group was consisted of mice that were targeted either at the hypothalamus or the right hemisphere, with PNPs range of 180 to 200 kPa (Fig. 21A).

Results for the 250 kHz center-frequency revealed that the mice group treated with MB + FUS + LNP versus the control groups (LNP only) showed a significant increase in total flux compared to the control group (* $p \leq 0.05$; Unpaired students t-test) (Fig. 21B). Specifically, there was a 10.9 ± 12.0 fold increase in signal compared to the LNP-only group (Fig. 21C). Due to the high variance observed, we sought to confirm the accuracy of the signal in both the control and treated groups through immunofluorescent staining. One brain from each group was sampled and stained with anti-Luc antibody and DAPI. The staining confirmed the respective absence and presence of luciferase protein expression in these brains (Fig. 21D).

Interestingly, comparison between the results of FUS-mediated BBBO for delivery and expression of mRNA-LUC-LNPs in the center-frequency of 850 kHz (12-fold increase) and center-frequency of 250 kHz (10.9-fold increase), revealed similar results (Unpaired students t-test). However, the unacceptably high variance observed at 250 kHz further supported the decision to proceed with experiments in GBM using the 850 kHz center frequency (Fig. 21E).

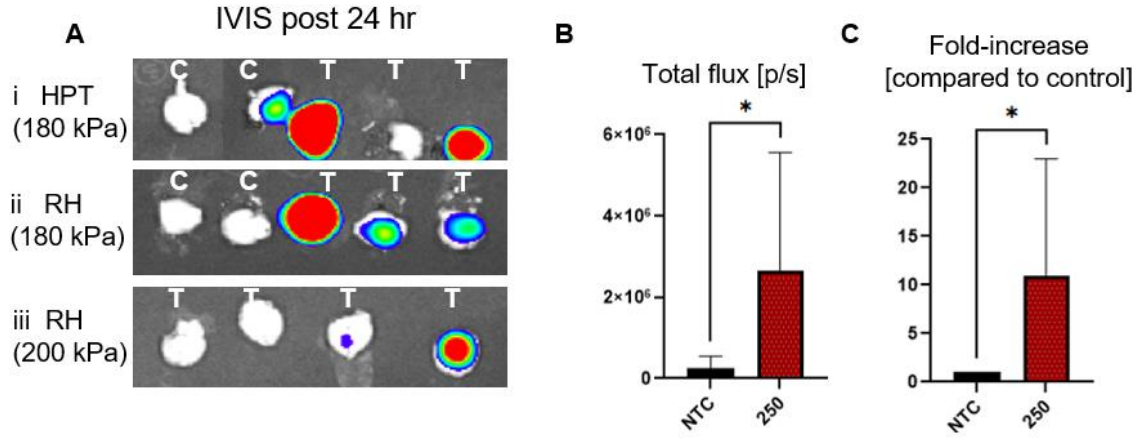

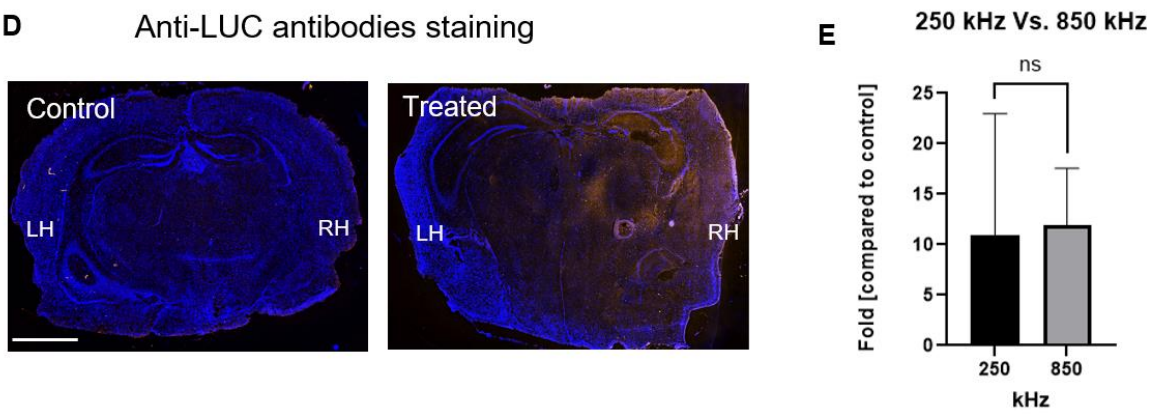

Figure 21. Luciferase protein expression post 24 hours. ***250 kHz center-frequency:*** (A) Bioluminescence images of whole brain mRNA-LUC-LNP (~100 nm) expression 24 hours post-BBBO, depicting different brain regions and PNP (abbreviations: HPT = hypothalamus, RH = right hemisphere, C = control, T = treated). (B) Comparison of total flux between the treated group (MB + FUS + LNP) and the control group (LNP only) in whole brains. (C) The graph in (B) presented as the fold increase in total flux compared to the control. (D) Fluorescence microscopy images of brain slices post-injection with mRNA-LUC-LNP after staining with anti-Luc antibody. Cell nuclei are stained with DAPI. The control group (LNP only) and the treated group (MB + FUS + LNP) are shown. RH (right hemisphere) and LH (left hemisphere) are indicated. Images were captured at 20x magnification. Scale bars: 2 mm. ***250 vs. 850 kHz center-frequency:*** (E) Comparison of the fold increase in total flux between 250 and 850 kHz. (B, C, E-) Unpaired students t-test ('ns' for not significant, * for $p<0.05$).

5.3. GBM mouse model

5.3.1. siRNA-Cy5-LNPs delivery

After establishing the capability to deliver LNPs to the brains of healthy mice, the ability to deliver the particles was tested in a GBM mouse model using the same parameters. BBBO was targeted to the RH of GBM bearing mice. The 005 GBM mouse model, closely mimics the human disease, and the tumor cells are GFP positive such that they fluoresce in green[75]. Fluorescence microscopy confirmed the delivery of siRNA-Cy5-LNP into the tumors (Fig. 22A). Comparison of mean intensity between the treated MBs + FUS + LNP and FUS+LNP control groups revealed a 6.7-fold increase in LNP fluorescence signal within the tumor region in treated brains compared to the controls (78.9 ± 28.0 a.u. vs 11.76 ± 3.29 a.u., *** $p \leq 0.001$; Unpaired students t-test) (Fig. 22B). Confocal microscopy (x40 magnification) confirmed the co-localization of siRNA-Cy5-LNP signal in the red channel with the 005 GBM cells

signal in the green channel (Fig. 22C). The overlap with the blue channel (DAPI) in areas where there is no signal in the green channel suggests that the LNPs were also taken up by other cells in the tumor microenvironment or that there is a decay of the green channel signal as a function of time.

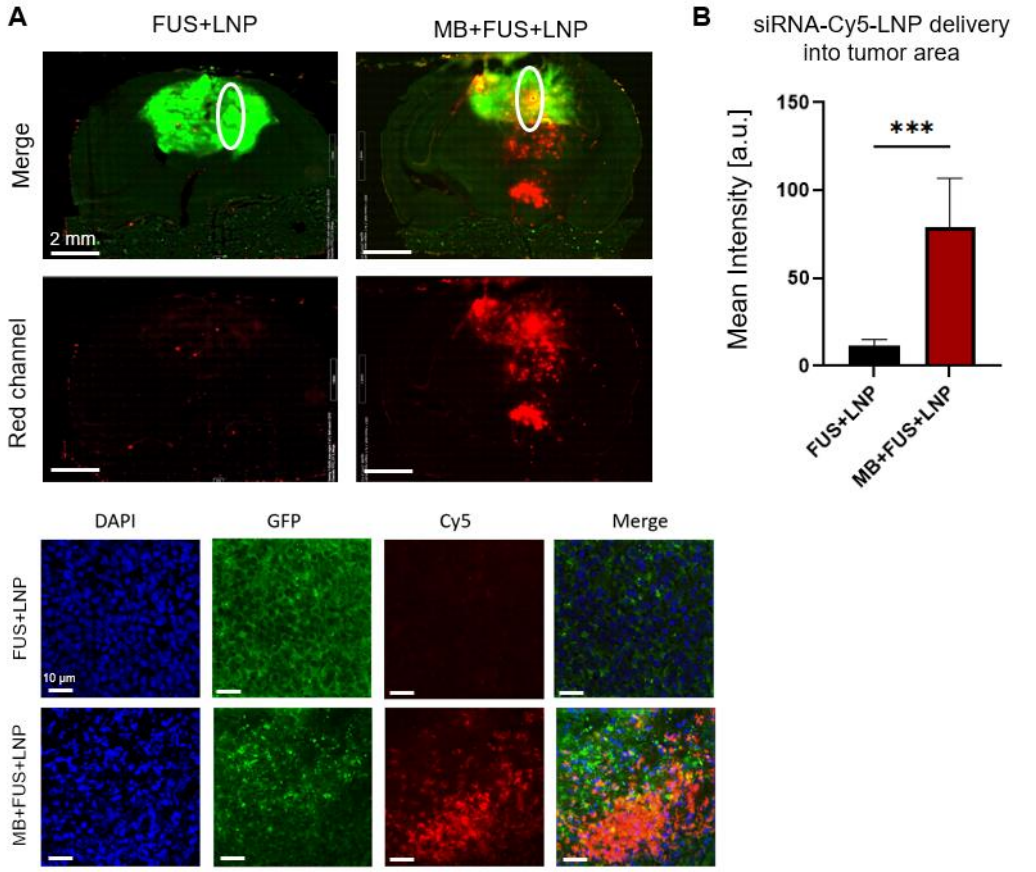

Figure 22. FUS-mediated BBBO for the delivery of siRNA-Cy5-LNP into glioblastoma tumors. (A) Fluorescence microcopy images of brain slices after BBBO showing delivery of siRNA-Cy5-LNP (~70 nm) in treated (FUS+LNP+MB) vs. control (FUS+LNP) GBM brains. Images were captured with a 20x magnification. Scale bar: 2mm. (B) Quantification of siRNA-Cy5-LNP fluorescence in treated compared to controls brains. (C) Confocal microscopy (x40 magnification) of the tumor region stained by DAPI. Green channel shows the GFP positive tumor cells and red channel is the siRNA-Cy5-LNP. Scale bar: 10 µm. (B) Unpaired students t-test (*** $p \leq 0.001$).

6. Discussion

This study investigates the use of low-frequency FUS-mediated BBBO with MBs to enhance the delivery of large particles, focusing specifically on mRNA-based LNP as a platform for future advanced non-invasive local brain therapies. In this work, we developed a robust platform for the noninvasive, safe, and efficient delivery of LNPs with diameters of ~70-100 nm to both healthy brain tissue and GBM tumors. To the best of our knowledge, this is the first demonstration of successful delivery of large LNPs to GBM tumors using FUS-mediated BBBO. This achievement addresses a critical gap in the clinical translation of LNPs, which are FDA-approved and widely recognized as advanced therapeutic agents but have not been used in brain therapies due to the challenges posed by the BBB. While there are 24 clinical trials underway using MB-enhanced ultrasound for gliomas, all focus on small molecules, leaving the potential of LNPs unexplored[44]. Our work demonstrates that LNPs, with their ability to encapsulate RNA-based therapeutics such as siRNA and mRNA, can now be safely delivered to the brain using a noninvasive approach. Additionally, our study presents a comprehensive evaluation of the delivery of a wide range of molecules and macromolecules, including small molecules, dextrans of varying sizes, and LNPs, enabling the identification of a unique set of parameters, that allow for the safe and efficient delivery of both small and large particles across the BBB.

Our results show that operating at a center-frequency of 850 kHz in a PNP of 125 kPa establishes a consistent threshold for safe and effective delivery of particles of various sizes, while preserving tissue integrity. This approach contrasts with prior studies that employed higher frequencies, that are less clinically relevant, resulting in size-dependent delivery, where the need for increased PNPs for larger particles is often limited by safety concerns[34,35,36,45,46]. Moreover, low frequencies offer improved skull penetration efficiency and enable wider focal coverage that can be suited for testing brain delivery. In this study FUS-mediated BBBO with MBs was tested in three low intensity center-frequencies (850, 250 and 80 kHz) by monitoring the extravasation of EB. A MB dose of 2×10^7 MBs per 20 g of body weight was chosen as it is consistent with our previous studies on BBBO to yield efficient BBBO[40–42], and falls within the commonly reported range used in BBBO studies in mice and according to the clinically approved dose of FDA-approved commercially available MBs[30,47]. Additionally, the

MBs used in this study were size-selected to remove bubbles larger than 5 µm, reducing size heterogeneity and enhancing safety. The use of an identical transducer operating at various frequencies allows for the study of frequency effects without altering other parameters such as aperture size or focal distance. This provides a platform for accurately examining the impact of ultrasound frequency on BBBO. The results presented distinct variation in the opening pattern and coverage area between the different center-frequencies. For each center-frequency, the initial PNP values were chosen based on previous studies or by using the PNP values established at other frequencies as a starting point for testing at lower frequencies. At 80 kHz, we initially tested 180 kPa based on values determined for the 250 kHz center frequency. However, this PNP caused safety concerns, so it was gradually reduced. At 90 kPa, strong BBBO was achieved across the majority of the brain, but microhemorrhages were observed. Further reduction to 75 kPa yielded mild BBBO without microhemorrhages. Based on these results, we concluded that 80 kHz is not an ideal frequency for focused and precise BBBO in the mouse model. At 250 kHz, BBBO was primarily observed at the edges of the brain near the skull (top and bottom), while minimal opening was seen in the center of the brain. This may be due to the phenomenon of standing waves contributing to the effect, suggesting that working with a larger animal model, such as a rat, could mitigate this impact[48]. Moreover, our original study from 2018 identified the safe range of PNPs as below 190 kPa, at which microhemorrhage was observed[39]. When replicating this with a new, identical transducer, we found that a PNP range of 180–200 kPa enabled safe and reproducible BBBO without microhemorrhages, as confirmed by fluorescence microscopy and histological analyses[41]. We believe that this slight variation (less than 15%) is likely due to hydrophone calibration differences and associated uncertainties. At 850 kHz, we started with a PNP of 500 kPa based on observations from studies conducted at a frequency of 1 MHz, where a PNP of was reported to effectively induce BBBO[49]. However, at a frequency of 850 kHz, microhemorrhages were observed at this PNP, prompting a stepwise reduction until a safe and effective BBBO was achieved at 125 kPa. This frequency was found optimal out of the three different frequencies that were tasted, with measured focal dimensions of 3.5 x 7 mm^2, providing a good coverage of the RH in a mouse brain. As such, this center frequency was chosen for the subsequent sonication experiments.

These optimized parameters (850 kHz, 125 kPa, duty cycle of 0.1%) were then

applied for the delivery of various-sized fluorescent dextrans (4, 70, 150 kDa) and two types of LNPs: fluorescent siRNA-Cy5-LNP and bioluminescent mRNA-luc-LNP. Comparative analysis of the fluorescent markers revealed a consistent opening area in X axis, and the strongest fold-increase in mean intensity observed for EB, followed by Dextran 150 kDa, which was the closest to the siRNA-Cy5-LNP (~70 nm). Interestingly, EB is a small molecule (~ 1kDa) known for its high binding to albumin, and 70 kDa dextran has a comparable size to the albumin-EB complex[50]. Our results revealed that EB penetration was much stronger than Dextran 70 kDa, suggesting the involvement of size-independent mechanisms in the delivery process.

For Cy5-siRNA-LNP delivery, it has been previously reported that larger particles typically require higher PNPs compared to smaller molecules for effective delivery[35,51]. These studies also indicate the potential for microhemorrhage at such PNPs. As a result, LNP delivery was initially tested at 300 kPa to balance delivery efficiency and safety, yet resulted in microhemorrhage as well. Consequently, the PNP was gradually decreased, and it was found that 125 kPa, the same PNP optimized for EB and other molecules, was sufficient for the safe and effective delivery of LNPs. This demonstrates the effectiveness of our low-frequency ultrasound protocol in enabling efficient delivery across a range of particle sizes while maintaining microvascular integrity. Next, in order to further validate the potential of LNPs as nanocarriers for mRNA encapsulation and gene expression manipulation, the delivery performance of mRNA-LNPs was assessed using bioluminescent mRNA-luc-LNP and subsequent luciferase expression measurement 24 hours post-treatment. The results demonstrated effective delivery exclusively in the FUS-mediated BBBO group with 12-fold delivery enhancement compared to the non-treatment control. Importantly, comparison of the treated group (MB + FUS + LNP) versus the three control groups (FUS + LNP, MB + LNP, and LNP) demonstrated that the enhancement in treatment efficacy is specifically attributable to the combined use of MB and FUS, with neither FUS nor MBs alone producing a significant effect. A limitation of our methodology is the need for brain extraction in order to analyze the delivery signal, therefore, the inability to trace BBB disruption at different time points in whole animals. Developing LNPs decorated with magnetic resonance-based contrast agents could enable the used of magnetic resonance imaging for the monitoring of BBBO. Another limitation is that measuring the fluorescent signal provides a qualitative assessment of the received signal. If further

quantification of LNP accumulation in brain tissue is desired, one potential method would be radiolabeling the LNPs, allowing precise measurement of their concentration in tumorous and normal brain tissues using gamma counting or autoradiography[52]. Alternatively, by loading the LNPs with a therapeutic RNA payload, its presence in the brain could be quantified using qRT-PCR or other RNA quantification techniques, such as RNA sequencing, to evaluate delivery efficiency[14,53].

Based on our optimization results, we assessed the delivery of fluorescent LNPs, targeting their delivery into the RH of the GBM syngeneic 005 mouse model, which closely mimics the human disease[43]. The signal observed in the treated brains showed 6.7-fold increase compared to controls. Ultimately, FUS-mediated BBBO using the optimized parameters allowed the delivery of LNPs into the GBM brain tumors. The focal beam of the transducer used in this study (H-115, Sonic Concepts) covered most of the right hemisphere. By targeting the right hemisphere, we were able to use the left hemisphere as a control, a common methodology in assessments of BBBO[30]. However, within the right hemisphere, the beam covered both the tumor and adjacent healthy brain tissue, meaning that it was not exclusively targeted to the tumor. Instead, our focus was on identifying parameters that enable efficient delivery of LNPs to the tumors. To achieve precise targeting of the tumor alone, a tighter focus would be required. This can be achieved by using a larger aperture transducer, employing a higher frequency, or working with a larger animal model where such a focal spot is clinically relevant. Associated limitations would be that a smaller focal zone would also require beam steering (mechanically or electronically) to ensure complete coverage of the tumor. Additionally, this approach would necessitate image-guided methods, such as magnetic resonance-guided focused ultrasound, to detect the tumor and direct the ultrasound beam accurately. In this study, the tumors were injected stereotactically, and the large focal zone of the beam ensured sufficient spatial alignment with the tumor. An alternative approach to enhance targeting is to develop LNPs with therapeutic content specifically designed to target tumor cells or the tumor microenvironment. However, it may also be possible to design a particle that does not impair performance even when delivered to healthy tissue, making the use of a large focal spot advantageous. This approach could shorten treatment time and ensure complete treatment coverage of the tumor. In this study, our primary goal was to establish a noninvasive, safe, and efficient delivery platform for LNPs to both healthy brain tissue

and GBM tumors. Hence, the use of a large focal zone was beneficial for achieving this objective.

Here, we focused on a single BBBO treatment session to assess the delivery capabilities. The feasibility of repeated BBBO treatments depends on the therapeutic agent being delivered. For example, in cases involving one-time treatments such as CRISPR[14] or AAV[54], a single BBBO may suffice. However, for therapies requiring periodic administration, such as chemotherapy, repeated BBBO treatments would be necessary. The feasibility of repeated treatments has been demonstrated in previous non-human primates studies[55], showing that BBBO can be performed multiple times without significant adverse effects. Furthermore, currently there are 24 interventional clinical trials listed on ClinicalTrials.gov, focusing on monthly BBBO treatments accompanying the chemotherapy cycles, with few of them completed showing promising results[44,56]. In future work, testing the safety of our parameters in consecutive cycles, and the impact of repeated treatments of therapeutic RNA-loaded LNPs on tumor progression and therapeutic outcomes is also warranted.

While GBM serves as a representative model in our study, the potential of the method extends far beyond this specific pathology. FUS-mediated BBBO represents a promising avenue for addressing a spectrum of neurological conditions, including Alzheimer's disease, Parkinson's disease, psychiatric disorders, and chemotherapy/antibody-based treatment in GBM[23–26]. Traditional approaches to overcoming the BBB often rely on drug mechanisms tailored to specific neurological disorders, limiting their efficacy. Specifically, in brain cancer treatment, local chemotherapy administration into shunted tumors remains a common yet invasive procedure fraught with complications and the development of chemotherapy resistance, highly the need for new therapeutic approaches[57].

The LNPs delivered in this study are capable of efficiently encapsulate modifying-messenger RNA to manipulate gene expression[14,58], outperform the efficiency and safety of their alternatives such as adeno-associated viruses (AAVs) and plasmid DNA (pDNA), hence the considerable interest in their use[9]. Their high performance was demonstrated in the development of mRNA vaccines for COVID-19 pandemic[11,59–61]. In addition, they not only enable the delivery of therapeutic mRNA sequences but also facilitates the co-delivery of dye-RNA-conjugated tracers for

visualization of extravasation in the brain, potentially enhancing theranostic approaches[62].

In conclusion, this paper is a comprehensive evaluation of a technology platform for the noninvasive delivery of LNPs to the brain via FUS-mediated BBBO. This work represents a significant step forward in enabling the noninvasive delivery of brain advanced therapeutic platforms. While the therapeutic efficacy of encapsulated RNA payloads in treating GBM tumors is beyond the scope of the current study, it is a key direction for future research. Consequentially, further studies, particularly efficacy and survival studies, are needed. Ultimately, our goal is to translate these promising results into tangible clinical benefits for patients suffering from neurological conditions, thereby addressing a critical unmet need in neurotherapeutics.

7. Final conclusions and future work

In conclusion, this thesis is a comprehensive evaluation of non-invasive brain drug-delivery platform as a step towards future brain therapies. Nevertheless, further studies, particularly efficacy and survival studies, are needed. These studies will provide critical insights into the long-term effects of therapeutic RNA-based LNPs on disease progression and overall survival in diverse neurological disease models, thereby informing future clinical translation efforts. Our findings set the stage for future research endeavors aimed at optimizing LNP formulations, exploring different therapeutic RNA sequences, and conducting additional preclinical nanomedicine studies across various neurological disorders. Ultimately, our goal is to translate these promising results into tangible clinical benefits for patients suffering from neurological conditions, thereby addressing a critical unmet need in neurotherapeutics.

8. References

1. Haddad-Tóvolli, R., Dragano, N. R. V, Ramalho, A. F. S. & Velloso, L. A. Development and function of the blood-brain barrier in the context of metabolic control. *Front Neurosci* **11**, 261080 (2017).
2. Pandit, R., Chen, L. & Götz, J. The blood-brain barrier: Physiology and strategies for drug delivery. *Adv Drug Deliv Rev* **165**, 1–14 (2020).
3. Daneman, R. & Prat, A. The blood–brain barrier. *Cold Spring Harb Perspect Biol* **7**, a020412 (2015).
4. Pardridge, W. M. The blood-brain barrier: bottleneck in brain drug development. *NeuroRx* **2**, 3–14 (2005).
5. Angom, R. S., Nakka, N. M. R. & Bhattacharya, S. Advances in Glioblastoma Therapy: An Update on Current Approaches. *Brain Sci* **13**, 1536 (2023).
6. Sweeney, M. D., Sagare, A. P. & Zlokovic, B. V. Blood–brain barrier breakdown in Alzheimer disease and other neurodegenerative disorders. *Nat Rev Neurol* **14**, 133–150 (2018).
7. Arvanitis, C. D., Ferraro, G. B. & Jain, R. K. The blood–brain barrier and blood–tumour barrier in brain tumours and metastases. *Nat Rev Cancer* **20**, 26–41 (2020).
8. Van Tellingen, O. *et al.* Overcoming the blood–brain tumor barrier for effective glioblastoma treatment. *Drug Resistance Updates* **19**, 1–12 (2015).
9. Jeong, M., Lee, Y., Park, J., Jung, H. & Lee, H. Lipid nanoparticles (LNPs) for in vivo RNA delivery and their breakthrough technology for future applications. *Adv Drug Deliv Rev* 114990 (2023).
10. Suzuki, Y. & Ishihara, H. Difference in the lipid nanoparticle technology employed in three approved siRNA (Patisiran) and mRNA (COVID-19 vaccine) drugs. *Drug Metabolism and Pharmacokinetics* vol. 41 Preprint at https://doi.org/10.1016/j.dmpk.2021.100424 (2021).
11. Teo, S. P. Review of COVID-19 mRNA Vaccines: BNT162b2 and mRNA-1273. *Journal of Pharmacy Practice* vol. 35 947–951 Preprint at https://doi.org/10.1177/08971900211009650 (2022).
12. Palucka, A. K. & Coussens, L. M. The Basis of Oncoimmunology. *Cell* vol. 164 1233–1247 Preprint at https://doi.org/10.1016/j.cell.2016.01.049 (2016).

13. Rosenblum, D. *et al. CRISPR-Cas9 Genome Editing Using Targeted Lipid Nanoparticles for Cancer Therapy*. *Sci. Adv* vol. 6 https://www.science.org (2020).
14. CHMP. *ANNEX I SUMMARY OF PRODUCT CHARACTERISTICS*.
15. Wu, S.-K. *et al.* Characterization of different microbubbles in assisting focused ultrasound-induced blood-brain barrier opening. *Sci Rep* **7**, 46689 (2017).
16. Hynynen, K., McDannold, N., Sheikov, N. A., Jolesz, F. A. & Vykhodtseva, N. Local and reversible blood–brain barrier disruption by noninvasive focused ultrasound at frequencies suitable for trans-skull sonications. *Neuroimage* **24**, 12–20 (2005).
17. Hynynen, K. & Jones, R. M. Image-guided ultrasound phased arrays are a disruptive technology for non-invasive therapy. *Phys Med Biol* **61**, R206 (2016).
18. McDannold, N., Arvanitis, C. D., Vykhodtseva, N. & Livingstone, M. S. Temporary disruption of the blood–brain barrier by use of ultrasound and microbubbles: safety and efficacy evaluation in rhesus macaques. *Cancer Res* **72**, 3652–3663 (2012).
19. Hynynen, K., McDannold, N., Vykhodtseva, N. & Jolesz, F. A. Noninvasive MR imaging–guided focal opening of the blood-brain barrier in rabbits. *Radiology* **220**, 640–646 (2001).
20. Meng, Y. *et al.* Safety and efficacy of focused ultrasound induced blood-brain barrier opening, an integrative review of animal and human studies. *Journal of controlled release* **309**, 25–36 (2019).
21. Pelekanos, M. *et al.* Establishing sheep as an experimental species to validate ultrasound-mediated blood-brain barrier opening for potential therapeutic interventions. *Theranostics* **8**, 2583 (2018).
22. Meng, Y., Hynynen, K. & Lipsman, N. Applications of focused ultrasound in the brain: from thermoablation to drug delivery. *Nat Rev Neurol* **17**, 7–22 (2021).
23. Leinenga, G., Langton, C., Nisbet, R. & Götz, J. Ultrasound treatment of neurological diseases—current and emerging applications. *Nat Rev Neurol* **12**, 161–174 (2016).
24. Carpentier, A. *et al.* Clinical trial of blood-brain barrier disruption by pulsed ultrasound. *Sci Transl Med* **8**, 343re2-343re2 (2016).

25. Liu, H.-L. *et al.* Focused ultrasound enhances central nervous system delivery of bevacizumab for malignant glioma treatment. *Radiology* **281**, 99–108 (2016).
26. Arrieta, V. A. *et al.* Ultrasound-mediated delivery of doxorubicin to the brain results in immune modulation and improved responses to PD-1 blockade in gliomas. *Nat Commun* **15**, (2024).
27. Noroozian, Z. *et al.* MRI-guided focused ultrasound for targeted delivery of rAAV to the brain. *Adeno-Associated Virus Vectors: Design and Delivery* 177–197 (2019).
28. Alonso, A. *et al.* Focal delivery of AAV2/1-transgenes into the rat brain by localized ultrasound-induced BBB opening. *Molecular Therapy-Nucleic Acids* **2**, (2013).
29. Morse, S. V, Mishra, A., Chan, T. G., de Rosales, R. T. M. & Choi, J. J. Liposome delivery to the brain with rapid short-pulses of focused ultrasound and microbubbles. *Journal of Controlled Release* **341**, 605–615 (2022).
30. Kheirolomoom, A. *et al.* Acoustically-active microbubbles conjugated to liposomes: Characterization of a proposed drug delivery vehicle. *Journal of Controlled Release* **118**, 275–284 (2007).
31. Ogawa, K. *et al.* Efficient gene transfection to the brain with ultrasound irradiation in mice using stabilized bubble lipopolyplexes prepared by the surface charge regulation method. *Int J Nanomedicine* 2309–2320 (2018).
32. Burgess, A. *et al.* Targeted delivery of neural stem cells to the brain using MRI-guided focused ultrasound to disrupt the blood-brain barrier. *PLoS One* **6**, e27877 (2011).
33. Valdez, M. A., Fernandez, E., Matsunaga, T., Erickson, R. P. & Trouard, T. P. Distribution and diffusion of macromolecule delivery to the brain via focused ultrasound using magnetic resonance and multispectral fluorescence imaging. *Ultrasound Med Biol* **46**, 122–136 (2020).
34. Chen, H. & Konofagou, E. E. The size of blood–brain barrier opening induced by focused ultrasound is dictated by the acoustic pressure. *Journal of Cerebral Blood Flow & Metabolism* **34**, 1197–1204 (2014).
35. Urbanczyk, M., Zbinden, A. & Schenke-Layland, K. Organ-specific endothelial cell heterogenicity and its impact on regenerative medicine and biomedical

engineering applications. *Advanced Drug Delivery Reviews* vol. 186 Preprint at https://doi.org/10.1016/j.addr.2022.114323 (2022).

36. Heye, A. K., Culling, R. D., Valdés Hernández, M. D. C., Thrippleton, M. J. & Wardlaw, J. M. Assessment of blood-brain barrier disruption using dynamic contrast-enhanced MRI. A systematic review. *NeuroImage: Clinical* vol. 6 262–274 Preprint at https://doi.org/10.1016/j.nicl.2014.09.002 (2014).
37. Saunders, N. R., Dziegielewska, K. M., Møllgård, K. & Habgood, M. D. Markers for blood-brain barrier integrity: How appropriate is Evans blue in the twenty-first century and what are the alternatives? *Frontiers in Neuroscience* vol. 9 Preprint at https://doi.org/10.3389/fnins.2015.00385 (2015).
38. Xu, Y. *et al.* Quantifying blood-brain-barrier leakage using a combination of evans blue and high molecular weight FITC-Dextran. *J Neurosci Methods* **325**, (2019).
39. Plaksin, M. *et al.* Magnetic resonance imaging analysis predicts nanoparticle concentration delivered to the brain parenchyma. *Commun Biol* **5**, (2022).
40. Ku, M.-C., Waiczies, S., Niendorf, T. & Pohlmann, A. Assessment of Blood Brain Barrier Leakage with Gadolinium-Enhanced MRI. in *Preclinical MRI: Methods and Protocols* (eds. García Martín, M. L. & López Larrubia, P.) 395–408 (Springer New York, New York, NY, 2018). doi:10.1007/978-1-4939-7531-0_23.
41. Ilovitsh, T. *et al.* Enhanced microbubble contrast agent oscillation following 250 kHz insonation. *Sci Rep* **8**, 16347 (2018).
42. Villamiel, M., Montilla, A., García-Pérez, J. V, Cárcel, J. A. & Benedito, J. *Basic Principles of Ultrasound*. (John Wiley & Sons, Ltd, 2017). doi:10.1002/9781118964156.
43. Ensminger, D. & Bond, L. J. *Ultrasonics: Fundamentals, Technologies, and Applications*. (CRC press, 2024).
44. Speed, C. A. *Therapeutic Ultrasound in Soft Tissue Lesions*.
45. Diederich, C. J. Thermal ablation and high-temperature thermal therapy: Overview of technology and clinical implementation. in *International Journal of Hyperthermia* vol. 21 745–753 (2005).

46. Lingéman, J. E., McAteer, J. A., Gnessin, E. & Evan, A. P. Shock wave lithotripsy: Advances in technology and technique. *Nature Reviews Urology* vol. 6 660–670 Preprint at https://doi.org/10.1038/nrurol.2009.216 (2009).
47. Mathias, W. *et al.* Sonothrombolysis in ST-segment elevation myocardial infarction treated with primary percutaneous coronary intervention. *J Am Coll Cardiol* **73**, 2832–2842 (2019).
48. Bismuth, M. *et al.* Acoustically detonated microbubbles coupled with low frequency insonation: Multiparameter evaluation of low energy mechanical ablation. *Bioconjug Chem* **33**, 1069–1079 (2021).
49. Bismuth, M. *et al.* Low frequency nanobubble-enhanced ultrasound mechanotherapy for noninvasive cancer surgery. *Nanoscale* **14**, 13614–13627 (2022).
50. Riis, T. S., Webb, T. D. & Kubanek, J. Acoustic properties across the human skull. *Ultrasonics* **119**, (2022).
51. Hynynen, K. & Jolesz, F. A. *PII S0301-5629(97)00269-X • Original Contribution DEMONSTRATION OF POTENTIAL NONINVASIVE ULTRASOUND BRAIN THERAPY THROUGH AN INTACT SKULL*. (1998).
52. Shinar, H. & Ilovitsh, T. Volumetric Passive Acoustic Mapping and Cavitation Detection of Nanobubbles under Low-Frequency Insonation. *ACS Materials Au* (2024).
53. Yan, L., Fu, K., Li, L., Li, Q. & Zhou, X. Potential of sonobiopsy as a novel diagnosis tool for brain cancer. *Molecular Therapy Oncology* vol. 32 Preprint at https://doi.org/10.1016/j.omton.2024.200840 (2024).
54. Wasielewska, J. M. & White, A. R. "Focused Ultrasound-mediated Drug Delivery in Humans – a Path Towards Translation in Neurodegenerative Diseases". *Pharmaceutical Research* vol. 39 427–439 Preprint at https://doi.org/10.1007/s11095-022-03185-2 (2022).
55. Miller, D. L. Overview of experimental studies of biological effects of medical ultrasound caused by gas body activation and inertial cavitation. *Progress in Biophysics and Molecular Biology* vol. 93 314–330 Preprint at https://doi.org/10.1016/j.pbiomolbio.2006.07.027 (2007).

56. Ohta, S. *et al.* Investigating the optimum size of nanoparticles for their delivery into the brain assisted by focused ultrasound-induced blood–brain barrier opening. *Sci Rep* **10**, (2020).
57. Gattegno, R. *et al.* Enhanced capillary delivery with nanobubble-mediated blood-brain barrier opening and advanced high resolution vascular segmentation. *Journal of Controlled Release* **369**, 506–516 (2024).
58. Katz, S. *et al.* Diameter-dependent assessment of microvascular leakage following ultrasound-mediated blood-brain barrier opening. *iScience* **26**, (2023).
59. Veiga, N. *et al.* Cell specific delivery of modified mRNA expressing therapeutic proteins to leukocytes. *Nat Commun* **9**, (2018).
60. Louis, D. N. *et al.* The 2007 WHO classification of tumours of the central nervous system. *Acta Neuropathologica* vol. 114 97–109 Preprint at https://doi.org/10.1007/s00401-007-0243-4 (2007).
61. Wu, W. *et al.* Glioblastoma multiforme (GBM): An overview of current therapies and mechanisms of resistance. *Pharmacol Res* **171**, 105780 (2021).
62. Gao, J., Zhao, L., Wan, Y. Y. & Zhu, B. Mechanism of action of IL-7 and its potential applications and limitations in cancer immunotherapy. *International Journal of Molecular Sciences* vol. 16 10267–10280 Preprint at https://doi.org/10.3390/ijms160510267 (2015).
63. Fritzell, S. *et al.* IFNγ in combination with IL-7 enhances immunotherapy in two rat glioma models. *J Neuroimmunol* **258**, 91–95 (2013).
64. Aoki, T. *et al. Expression of Murine Interleukin 7 in a Murine Glioma Cell Line Results in Reduced Tumorigenicity in Vivo*. *Immunology* vol. 89 https://www.pnas.org (1992).
65. Jicha, D. L., Mul~, J. J. & Rosenberg, S. A. *Interleukin 7 Generates Antitumor Cytotoxic T Lymphocytes against Murine Sarcomas with Efficacy in Cellular Adoptive Immunotherapy*. http://rupress.org/jem/article-pdf/174/6/1511/1672899/1511.pdf?casa_token=NTsZfZoS9mcAAAAA:Ic39e1Q7W1Kww2eFUxSEano4oKVOcFJaOCu-l2L4RhJEn2VhZ9buWtdTzfUzUqD5P-MROlQ.
66. Gunnarsson, S. *et al.* Intratumoral IL-7 delivery by mesenchymal stromal cells potentiates IFNγ-transduced tumor cell immunotherapy of experimental glioma. *J Neuroimmunol* **218**, 140–144 (2010).

67. Murphy, W. J. *et al.* Antitumor effects of interleukin-7 and adoptive immunotherapy on human colon carcinoma xenografts. *Journal of Clinical Investigation* **92**, 1918–1924 (1993).
68. Fry, T. J. & Mackall, C. L. *Interleukin-7: From Bench to Clinic*. http://ashpublications.org/blood/article-pdf/99/11/3892/1685394/h81102003892.pdf (2002).
69. Sportès, C. *et al.* Administration of rhIL-7 in humans increases in vivo TCR repertoire diversity by preferential expansion of naive T cell subsets. *Journal of Experimental Medicine* **205**, 1701–1714 (2008).
70. Zhang, H. *et al.* Ultrasound molecular imaging of tumor angiogenesis with a neuropilin-1-targeted microbubble. *Biomaterials* **56**, 104–113 (2015).
71. Naidu, G. S. *et al.* A Combinatorial Library of Lipid Nanoparticles for Cell Type-Specific mRNA Delivery. *Advanced Science* **10**, 2301929 (2023).
72. Pulaski, B. A. & Ostrand-Rosenberg, S. Mouse 4T1 breast tumor model. *Curr Protoc Immunol* **39**, 20–22 (2000).
73. Peko, L., Katz, S., Gattegno, R. & Ilovitsh, T. Protocol to assess extravasation of fluorescent molecules in mice after ultrasound-mediated blood-brain barrier opening. *STAR Protoc* **5**, (2024).
74. Marumoto, T. *et al.* Development of a novel mouse glioma model using lentiviral vectors. *Nat Med* **15**, 110–116 (2009).
75. Chaichana, K. L., Pinheiro, L. & Brem, H. Delivery of local therapeutics to the brain: working toward advancing treatment for malignant gliomas. *Ther Deliv* **6**, 353–369 (2015).
76. Arsiwala, T. A. *et al.* Characterization of passive permeability after low intensity focused ultrasound mediated blood–brain barrier disruption in a preclinical model. *Fluids Barriers CNS* **19**, 72 (2022).
77. Choi, J. J., Wang, S., Tung, Y.-S., Morrison III, B. & Konofagou, E. E. Molecules of various pharmacologically-relevant sizes can cross the ultrasound-induced blood-brain barrier opening in vivo. *Ultrasound Med Biol* **36**, 58–67 (2010).
78. O'Reilly, M. A., Huang, Y. & Hynynen, K. The impact of standing wave effects on transcranial focused ultrasound disruption of the blood-brain barrier in a rat model. *Phys Med Biol* **55**, 5251–5267 (2010).

79. Chen, H. *et al.* Chemical conjugation of evans blue derivative: A strategy to develop long-acting therapeutics through albumin binding. *Theranostics* **6**, 243–253 (2016).
80. Heurling, K. *et al.* Quantitative positron emission tomography in brain research. *Brain Research* vol. 1670 220–234 Preprint at https://doi.org/10.1016/j.brainres.2017.06.022 (2017).
81. Horodyckid, C. *et al.* Safe long-term repeated disruption of the blood-brain barrier using an implantable ultrasound device: a multiparametric study in a primate model. *J Neurosurg* **126**, 1351–1361 (2017).
82. Sun, D. & Lu, Z. R. Structure and Function of Cationic and Ionizable Lipids for Nucleic Acid Delivery. *Pharmaceutical Research* vol. 40 27–46 Preprint at https://doi.org/10.1007/s11095-022-03460-2 (2023).
83. Tarab-Ravski, D. *et al.* Delivery of Therapeutic RNA to the Bone Marrow in Multiple Myeloma Using CD38-Targeted Lipid Nanoparticles. *Advanced Science* **10**, (2023).
84. Fang, E. *et al.* Advances in COVID-19 mRNA vaccine development. *Signal Transduction and Targeted Therapy* vol. 7 Preprint at https://doi.org/10.1038/s41392-022-00950-y (2022).
85. Schoenmaker, L. *et al.* mRNA-lipid nanoparticle COVID-19 vaccines: Structure and stability. *International Journal of Pharmaceutics* vol. 601 Preprint at https://doi.org/10.1016/j.ijpharm.2021.120586 (2021).
86. Sahin, U. *et al.* COVID-19 vaccine BNT162b1 elicits human antibody and TH1 T cell responses. *Nature* **586**, 594–599 (2020).
87. Naziris, N. & Demetzos, C. Lipid nanoparticles as platforms for theranostic purposes: recent advances in the field. *Journal of Nanotheranostics* **3**, 86–101 (2022).

9. תקציר

ננו-חלקיקים ליפידיים משמשים כמערכת מתקדמת להובלת רנ"א, אשר אושרה על ידי ה FDA לשימוש בטיפולים של ריפוי גנטי ואימונותרפיה. למרות הפוטנציאל שיש לפלטפורמה לטיפול במוח, יכולת ההעברה המערכתית של החלקיקים הליפידיים אל המוח מוגבל עקב קיום מחסום-הדם-מוח, שמונע מעבר של תרופות אשר גודלן עולה על 0.4 קילודלתון מהדם אל המוח. הטכנולוגיה של אולטרסאונד ממוקד בשילוב מיקרובועות נחשבת למובילה בפתיחת מחסום-דם-מוח באופן מקומי, בטוח והפיך. עם זאת, העברה של חלקיקים גדולים נותרה אתגר, מכיוון שפתיחה מספקת של המחסום להעברת חלקיקים גדולים גוררת לרוב העלאת לחץ האולטרסאונד שמופעל והדבר עלול לגרום לפגיעה בכלי הדם והרקמה המוחית. במחקר זה, ביקשנו לאתגר את הפרדיגמה של העברת חלקיקים תלוית גודל. באמצעות אופטימיזציה מדויקת של פרמטרי אולטרסאונד בתדרים נמוכים, פיתחנו שיטה להעברת מגוון מולקולות גדולות, כולל ננו-חלקיקים ליפידיים, תחת אותם תנאי לחץ, מבלי לגרום לנזק לרקמות. בשלב הראשון, הערכנו את פתיחת מחסום-הדם-מוח במגוון תדרים (80, 250, ו-850 קילוהרץ) ולחצים שונים, על ידי מעקב אחר זליגת הסמן הפלורסנטי Evans blue (EB) לתוך רקמת המוח לאחר הזרקה מערכתית לזרם הדם. הפרמטרים האופטימליים לפתיחת המחסום אופיינו בתדר של 850 קילוהרץ ובלחץ של 125 קילופסקל.

בשלב הבא, השתמשנו בפרמטרים אלו להעברת מולקולות בגדלים שונים: דקסטרנים בגודל 4, 70 ו-150 קילודלתון, ושני סוגי ננו-חלקיקים ליפידיים: siRNA-Cy5-LNP (כ-70 ננומטר) וmRNA-luc-LNP- (כ-100 ננומטר). העברת המולקולות נבדקה באמצעות מיקרוסקופיה פלורסנטית וביולומיניסנציה (bioluminescence) בהתאמה. לבסוף, הדגמנו העברה של siRNA-Cy5-LNP במודל עכברי של גליובלסטומה אגרסיבית מסוג 005 דרך מחסום הדם-מוח ואל הגידול.

תוצאות המחקר בעכברים הדגימו העברה בטוחה ויעילה הן של מולקולות קטנות והן של ננו-חלקיקים ליפידיים גדולים תחת התנאים האופטימליים. בעכברים בריאים, פתיחת מחסום-דם-מוח להעברת חלקיקים פלורסנטיים מסוג siRNA-Cy5-LNP הראתה עלייה של פי 10 בסיגנל בהשוואה למוחות ביקורת. בצורה דומה, העברת חלקיקים ביולומיניסנטיים (מקודדים לאנזים לוציפראז) mRNA-luc-LNP הראתה עלייה של פי 12 בביטוי האנזים 24 שעות לאחר הטיפול, בהשוואה לביקורת. כמו כן, במודל הגליובלסטומה העברה של חלקיקי siRNA-Cy5-LNP הדגימה עלייה של פי 6.7 בסיגנל ביחס לקבוצת הביקורת. לממצאים אלו עשויות להיות השלכות משמעותיות בקידום העברת חלקיקים טיפוליים בגדלים ננומטריים אל המוח בצורה לא פולשנית ובטוחה. מחקר זה מציע פלטפורמה רב-תכליתית לטיפולי מוח מבוססי רנ"א, כאשר ניתן לבצע התאמות בתוכן רצף הרנ"א, ולכן סולל את הדרך לפיתוח ובחינת טיפולים חדשניים במגוון של מחלות נוירודגנרטיביות וממאירויות מוח.